JOURNAL OF PETROLOGY | VOLUME 53 | NUMBER 8 | PAGES 1537–1567 | 2012 | doi:10.1093/petrology/egs025

Magmatic Sulfide Formation by Reduction of Oxidized Arc Basalt

ANDREW G. TOMKINS*, KYLE C. REBRYNA, ROBERTO F. WEINBERG AND BRUCE F. SCHAEFER†

SCHOOL OF GEOSCIENCES, P.O. BOX 28E, MONASH UNIVERSITY, MELBOURNE, VIC. 3800, AUSTRALIA

RECEIVED JANUARY 11, 2011; ACCEPTED MARCH 6, 2012
ADVANCE ACCESS PUBLICATION APRIL 20, 2012

The Hidaka Metamorphic Belt, in southeastern Hokkaido, Japan, provides insights into how magmatic sulfide deposits may form through magma mixing deep within arcs. Here, a near-complete cross-section of arc crust is exposed, with large mafic igneous complexes preserved at deeper levels. Magmatic sulfide mineralization occurs within the Opirarukaomappu Gabbroic Complex (OGC), which preserves a record of crustal contamination of mafic magmas via assimilation and magma mixing involving introduction of crust-derived tonalite. Assimilation–fractional crystallization modelling suggests that the gabbro evolved through a combination of approximately 10 wt % mixing and 14 wt % fractional crystallization. Magmatic sulfides and associated gabbros, diorites and tonalites at this locality contain graphite, with carbon isotope signatures consistent with derivation from the surrounding partially melted carbonaceous shales. This indicates that crust-derived carbon was added to the mafic magma through the magma mixing and assimilation process. Sulfur isotope data suggest that sulfur was also added from crustal sources during assimilation and magma mixing. The relationships observed in the OGC suggest that intrusion of basalt into a segment of deep arc crust drove partial melting of carbonaceous metamorphic rocks, producing graphite-bearing felsic magmas with high reducing potential. Redox budget modelling shows that mixing of only small proportions of these magmas is sufficient to lower the oxidation state of oxidized basaltic magmas enough to induce sulfide saturation and consequent exsolution of immiscible sulfide melt. Magmatic sulfide deposits are likely to form by this reduction-induced sulfide saturation mechanism deep within other arcs where magma mixing is thought to be common.

KEY WORDS: *Arc Magmatism; sulfide; magma mixing; ore genesis*

INTRODUCTION

Magmatic sulfide deposits are, with the exception of Sudbury, generally considered to be the product of continental rifting (Naldrett, 2004). However, there are a small number of deposits found in subduction-related magmatic arcs. The best known of these is the Aguablanca deposit in Spain (Casquet *et al.*, 2001; Piña *et al.*, 2010), which is one of about 11 (including the example discussed here) known globally [most of which were summarized by Piña *et al.* (2010); but see also Thakurta *et al.* (2008)]. Because there have not yet been many large deposits found in arcs, the possibility of magmatic sulfide formation in this environment has received little attention. This perceived scarcity of magmatic sulfide deposits feeds back into the minerals industry such that there is minimal exploration focused on this setting, which in turn confirms the premise, as no new deposits are found. However, we do know that at least some arc magmas are not metal depleted, because porphyry Cu–Au deposits form in association with intermediate arc magmas, and some of these contain elevated concentrations of platinum group elements (PGE) (Tarkian & Stribrny, 1999), so one might ask the question: Why are magmatic sulfide deposits not commonly found in arcs; or are they perhaps more abundant than generally considered?

It is well known that when sulfide saturation is reached in mafic silicate magmas immiscible droplets of sulfide melt exsolve (Naldrett, 2004), which partition and concentrate chalcophile elements as segregation progresses (Goldschmidt, 1937; Peach *et al.*, 1990). Many intrinsic melt properties affect sulfur solubility in silicate melts: temperature, pressure, SiO_2 content, and FeO content are

*Corresponding author. Telephone: +61-3-99051643. Fax: +61-3-99054903. E-mail: andy.tomkins@monash.edu
†Present address: GEMOC National Key Centre, Department of Earth and Planetary Sciences, Macquarie University, NSW 2109, Australia.

among the most well characterized (Haughton *et al.*, 1974; Mavrogenes & O'Neill, 1999; Li *et al.*, 2001; O'Neill & Mavrogenes, 2002). It has been suggested that oxygen fugacity (fO_2) might also have a limited role in controlling sulfur solubility in reduced magmas (MacLean, 1969), although the validity of this idea has been questioned (O'Neill & Mavrogenes, 2002). However, for a given silicate magma composition, the solubility of sulfur in the silicate melt increases by about an order of magnitude (for basalts from ~0·15% to ~1·5%) between melts with $fO_2 \leq$ FMQ and those with $fO_2 \geq$ FMQ + 2, respectively, where FMQ is the fayalite–magnetite–quartz buffer (see Carroll & Rutherford, 1985, 1987; Luhr, 1990; Jugo *et al.*, 2005; Jugo, 2009). This solubility jump is thought to represent the change from sulfide to sulfate stability, sulfate being more soluble than sulfide (Jugo *et al.*, 2005). Many arc basalts are oxidized and sulfur-rich (e.g. Carroll & Rutherford, 1987). For example, the 1991 Pinatubo eruption discharged the largest SO_2 gas cloud ever measured and the sulfur in this eruption has been linked to magma mixing involving one arc magma component that was highly oxidized (Kress, 1997). We therefore hypothesize that if oxidized arc basalt, with high concentrations of dissolved sulfur as sulfate, could be reduced into the sulfide stability field, this would cause sulfide saturation, possibly leading to ore deposit formation.

This study investigates the above hypothesis by studying a mixed magma complex within the Hidaka Metamorphic Belt in southeastern Hokkaido, Japan (Fig. 1). The Hidaka Belt is thought to represent a near-complete cross-section of arc crust (Maeda & Kagami, 1996; Tsumura *et al.*, 1999), with large mafic igneous complexes preserved at deeper crustal levels. We describe a magmatic sulfide body that occurs within the Opirarukaomappu Gabbroic Complex (OGC) at the southern end of the Hidaka Belt, which preserves a record of crustal contamination of hydrous mafic magmas via assimilation and magma mixing. Field and petrographic observations, S and C isotopic data, and geochemical mass balance are used to show that a high proportion of reducing material was added to the mafic magma at this locality. We use this as the basis for presenting a new model for magmatic sulfide genesis in arcs.

TECTONICS AND REGIONAL GEOLOGY OF THE HIDAKA METAMORPHIC BELT, JAPAN

The southern part of the Tertiary Hidaka Metamorphic Belt has been interpreted to be an east-dipping cross-section of arc crust, with a complete section from the mid–lower to upper crust exposed (Maeda & Kagami, 1996; Tsumura *et al.*, 1999). The Hidaka Metamorphic Belt, the Cretaceous Kohistan Sequence in Afghanistan (Treloar *et al.*, 1996), and the Jurassic Talkeetna Arc Section in Alaska (Greene *et al.*, 2006) are the only known exposed, near-complete cross-sections of arc crust. The magmatic interactions observed in the intrusions of the Hidaka Metamorphic Belt therefore provide a rare and important natural library of deep-crustal magmatic processes in arcs.

Japan is affected by the tectonic activity of four plates: the Eurasian, North American, Pacific, and Philippine (Fig. 1 inset). The Hidaka Metamorphic Belt is located on Hokkaido, the northernmost of the four major islands of Japan, which is situated between the North American, Eurasian, and Pacific plates. Once part of the Kuril Arc (Tsumura *et al.*, 1999), the Hidaka Metamorphic Belt resulted from collision between the paleo-Japan arc–trench system and the paleo-Kuril arc–trench system (on the Eurasian plate and North American paleoplate margins, respectively; Fig. 1 inset; see also Komatsu *et al.*, 1989). Westward thrusting along the crustal-scale Hidaka Main Thrust drove uplift of the Hidaka Metamorphic Belt. Gabbroic intrusive bodies in the southern Hidaka Metamorphic Belt have calc-alkaline major element compositions, and abundant hydrous mineral phases (Ishihara & Terashima, 1985), which suggest arc-related genesis (Komatsu *et al.*, 1989; Kemp *et al.*, 2007).

Anhydrous tholeiitic mid-ocean ridge basalt (MORB)-like gabbros in the northern half of the Hidaka Belt formed at 18·5 ± 0·3 Ma, on the basis of U–Pb dating of zircon from the gabbros (Kemp *et al.*, 2007). In contrast, K–Ar dating indicates that the hydrous calc-alkaline gabbros of the southern Hidaka Belt formed at ~35 Ma (Ishihara & Terashima, 1985). The granulite domain in the northern Hidaka Metamorphic Belt shares the same age range as the MORB-like gabbros (Kemp *et al.*, 2007), implying that it had not been obducted from the Kuril Arc onto the Japan Arc before 18 Ma. However, sediments surrounding the Hidaka Metamorphic Belt clearly show that this arc sequence was obducted in the Miocene (Kimura, 1986), which implies that the major phases of activity associated with its collision, accretion, and uplift started and ended in the Mid- to Late Miocene. The Eurasian–North American–Pacific plate triple junction has since migrated south, with a current disputed location in the eastern Sea of Japan (Chapman & Solomon, 1976; Kato *et al.*, 2004).

The Hidaka Metamorphic Belt exposes rocks that formed at depths ranging from ~23 km to near-surface conditions (Komatsu *et al.*, 1994; Maeda & Kagami, 1996). However, the sequence is not entirely intact, with shearing and thrust fault truncation reducing the outcropping thickness to 16 km (Komatsu *et al.*, 1989). Nakanogawa Group metasedimentary rocks are exposed in a succession that gradually decreases in metamorphic grade from west to

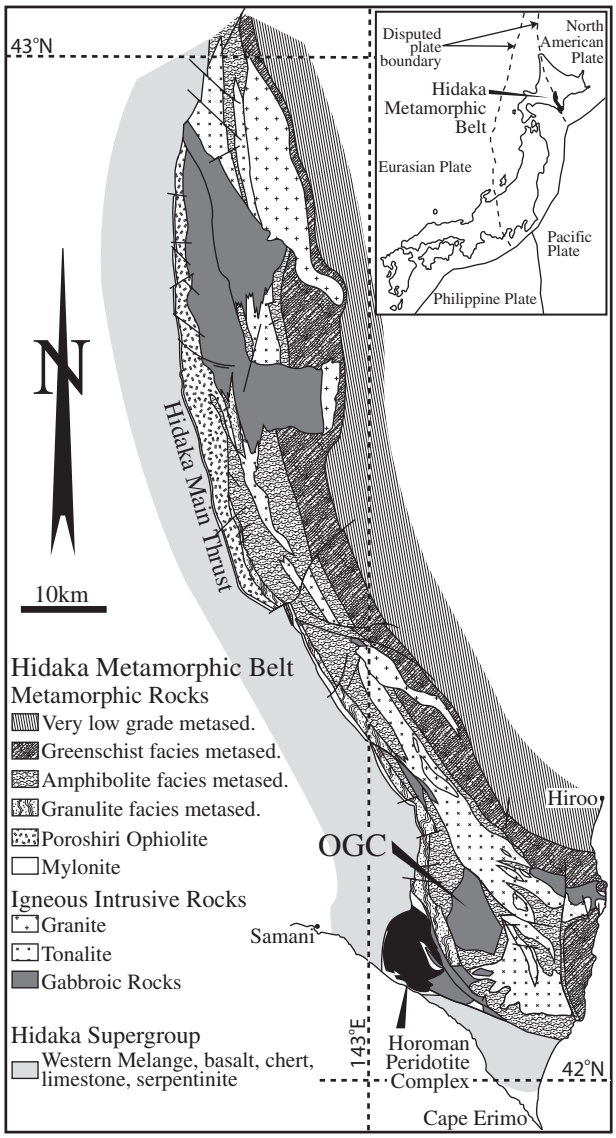

Fig. 1. Geological map of the Hidaka Metamorphic Belt, southeastern Hokkaido, Japan. Simplified from Owada *et al.* (2003). The location of the Opirarukaomappu Gabbroic Complex (OGC), which is detailed in Fig. 2, is shown.

east, representing progressively shallower levels in the arc crust, with granulite facies at the bottom through amphibolite and then greenschist facies near the top, situated conformably below nearly unmetamorphosed sediments (Fig. 1). The stratigraphic succession contains fault-bounded basal peridotite complexes, such as the Horoman Peridotite, which represents a portion of ancient lithospheric mantle (see Malaviarachchi *et al.*, 2008), ultramafic to mafic gabbros that lie within deep- to mid-crustal intrusive complexes (e.g. Kamiyama *et al.*, 2007), peraluminous and metaluminous tonalites, and granites at higher crustal levels. The OGC, which is the focus of the present study, is situated towards the southern end of the Hidaka Metamorphic Belt within the lower part of the crustal section (Fig. 1).

GEOLOGY OF THE OPIRARUKAOMAPPU GABBROIC COMPLEX

The OGC (Fig. 2) was emplaced into metasedimentary rocks of the Nakanogawa Group and has been uplifted from ~23 km depth (Komatsu *et al.*, 1989, 1994; Maeda & Kagami, 1996). Massive to disseminated sulfide mineralization occurs at the abandoned Horoman Ni–(Cu) mine

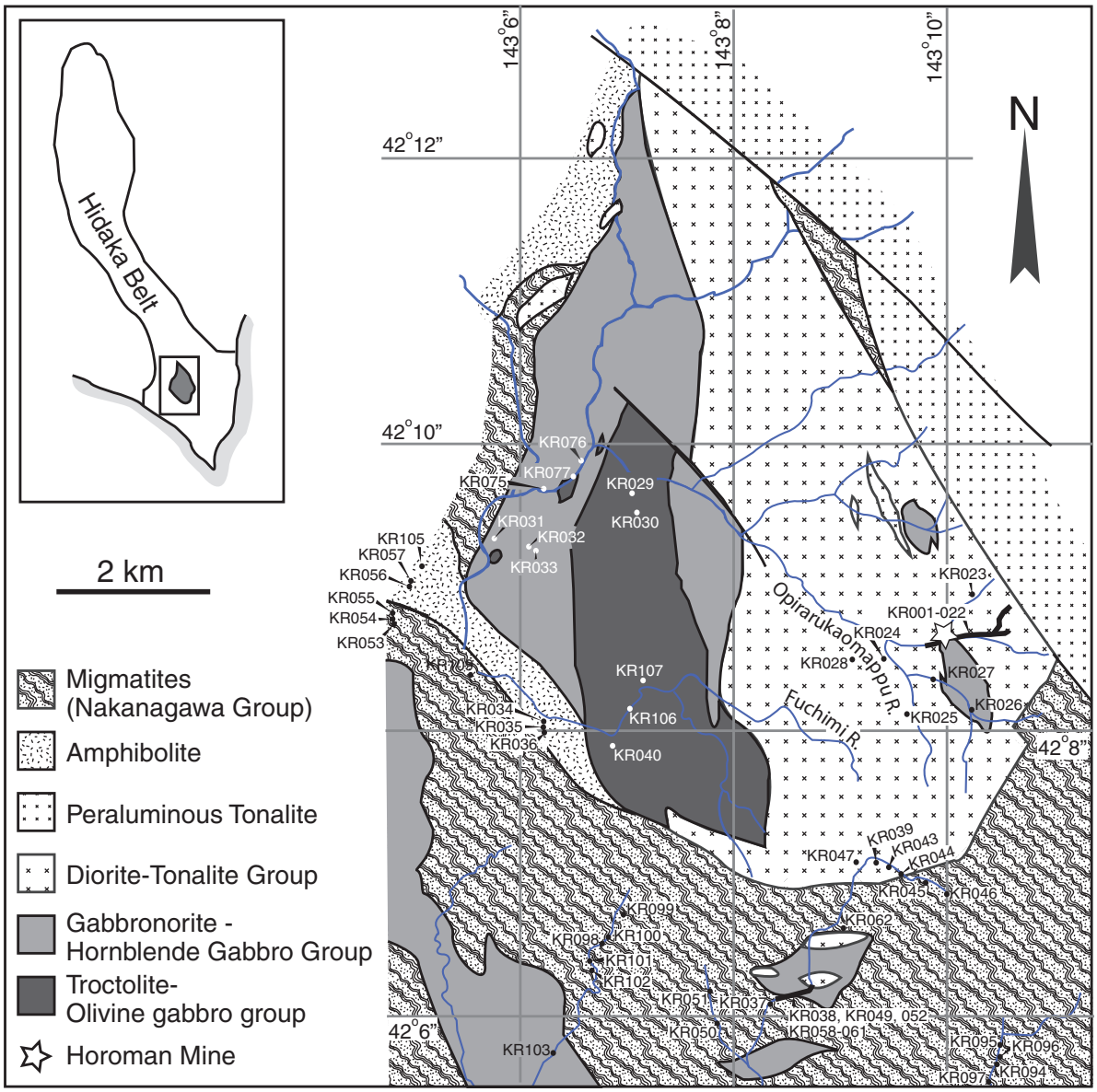

Fig. 2. Geological map of the Opirarukaomappu Gabbroic Complex (OGC) in the southern Hidaka Metamorphic Belt. Adapted from Honma (1997).

(Fig. 2), in association with a gabbronorite–hornblende gabbro described below. Several other small sulfide-rich occurrences occur in the eastern half of the OGC, and sparsely disseminated sulfides are a common feature of the more intermediate rocks of this region.

Honma (1997) described six distinct igneous units within the OGC: (1) a cumulate troctolite–olivine gabbro group, intruded by (2) fine-grained gabbronorite and (3) fine-grained olivine gabbronorite, (4) a gabbronorite–hornblende gabbro group, (5) a gabbro group, and (6) a diorite–tonalite group. Troctolite–olivine gabbros, gabbronorite–hornblende gabbros, and diorite–tonalite group rocks are the major units. On the basis of these units, the OGC may be broadly divided into two portions: troctolite–olivine gabbro and gabbronorite–hornblende gabbro in the western half, and diorite–tonalite in the eastern half (Fig. 2). In the vicinity of the Horoman Mine, and at other localities in the OGC, magma mingling textures between gabbro and tonalite are evident (Fig. 3), suggesting interaction between mantle- and crust-derived magmas.

Gabbroic rocks of the OGC

Troctolite and olivine gabbros constitute the most mafic compositions in the OGC, comprising approximately

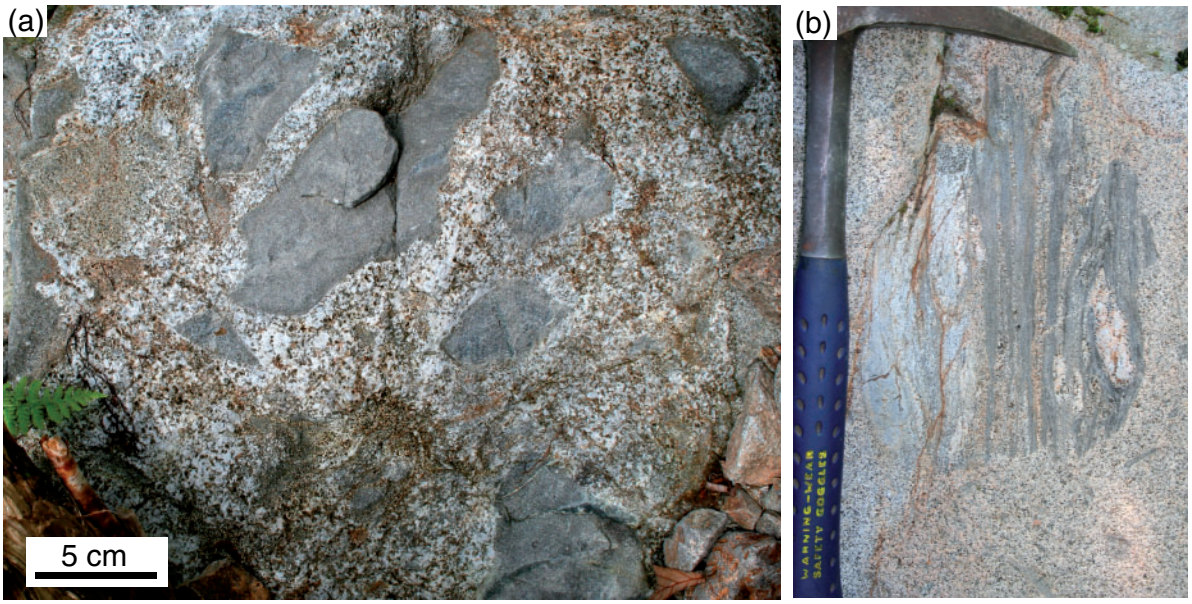

Fig. 3. Field photographs of the OGC. (a) Abundant gabbroic enclaves in tonalite are part of the observational evidence for magma mingling in the OGC. (b) An enclave of graphitic migmatitic Nakanagawa metasedimentary rock in host tonalite.

equal proportions of olivine ($\sim Fo_{75–80}$) and plagioclase ($\sim An_{70}$) (mineral compositions reported here were estimated by optical microscopy). These minerals are typically coarsely crystalline (>1 mm) and cumulate in texture. Olivine and pyroxenes (orthopyroxene and/or clinopyroxene) occur in more coarsely crystalline (~10 mm) samples, constituting up to 35% and 5%, respectively. Reaction rims occur between orthopyroxene and surrounding plagioclase and olivine, and commonly between olivine and plagioclase where orthopyroxene is located nearby. Olivine is locally twinned and plagioclase has pervasive albite twinning with weak normal zoning ($\sim An_{70}$ in cores to $\sim An_{35–40}$ in the rims). Opaque minerals form ~1% of the rock and are primarily pyrrhotite and chalcopyrite, with minor magnetite. Graphite was not observed in this unit.

The gabbronorite–hornblende gabbro group is the main sulfide-bearing unit in the OGC. Gabbronorite comprises roughly equal proportions (45%) of plagioclase and orthopyroxene, with some clinopyroxene, hornblende, and minor chlorite. Plagioclase ($\sim An_{50}$, 0·6 mm) has resorbed crystal margins, implying chemical instability with the final crystallization assemblage. Orthopyroxene is inclusion-rich and corroded. Clinopyroxene has rare simple twins, is partially replaced by hornblende, is typically anhedral against plagioclase crystals, and exhibits reaction rims against included plagioclase. Hornblende also contains plagioclase inclusions with reaction rims. All silicate phases are inclusion rich to the point of pervasive cloudiness. The opaque assemblage in the gabbronorite is dominated by pyrrhotite, with accessory chalcopyrite, pentlandite and ilmenite. Graphite is an accessory phase in many samples. Sulfide minerals are mainly distributed interstitially amongst the silicates, although some sulfide inclusions are hosted in clinopyroxene, and less commonly in plagioclase. Chlorite partially pseudomorphs hornblende in some samples, and is thought to be related to fluid infiltration brought about by obduction of the Hidaka Metamorphic Belt as it is paragenetically the latest phase. Leucogranite dikes cross-cut the gabbros in this region along fracture-controlled pathways.

Hornblende gabbros contain about 53% plagioclase (An_{45}) and 45% hornblende with minor biotite. The plagioclase features sieve textures and is slightly larger in grain size than the hornblende and biotite crystals. In some samples, hornblende has been replaced, to varying degrees, by biotite, which itself is slightly chloritized. The opaque assemblage in this rock type is almost entirely composed of ilmenite with rare sulfides (forming less than 1% of the total) and trace proportions of graphite. The opaque minerals are fine-grained (typically ≤0·15 mm), with the largest included in hornblende crystals and the smallest included in plagioclase. With plagioclase crystallizing first, it is likely that ilmenite saturation in the melt occurred synchronously with crystallization of the hornblende. In samples with more prevalent sulfides, the opaque minerals are most often included in or associated with biotite and hornblende.

Diorite–tonalite group

Diorites and tonalites of this group constitute the bulk of the eastern half of the OGC (Fig. 2). Hornblende diorites, and peraluminous and metaluminous tonalites are the major rock types in the diorite–tonalite group. Diorites

have plagioclase (~An_{38}) and hornblende as the dominant phases with biotite and quartz as minor phases. Plagioclase crystals range in size up to 1·1 mm, with hornblende, biotite, and quartz ranging in size up to 0·4 mm. Plagioclase is commonly sieve textured, but is not as inclusion-rich as in the gabbronorite and hornblende gabbros described above. The hornblende appears broadly unstable, having undergone varying degrees of replacement by biotite, and is generally resorbed in appearance. Biotite has undergone minor chloritization. Graphite is observed in some samples. Other opaque minerals are mostly ilmenite, with minor sulfide present, and are up to 1% in abundance. These phases occur mostly as inclusions in hornblende and biotite crystals.

Metaluminous tonalites have plagioclase (~An_{32}), quartz, biotite, and sometimes hornblende. Crystal sizes range up to 3·3 mm for plagioclase and up to 1 mm for quartz, biotite and hornblende. Plagioclase features normal zoning and mild sericitization with abundant inclusions. Myrmekite occurs throughout. Hornblende is rare in most samples and is usually highly resorbed. Graphite is observed in some hornblende-bearing and hornblende-free samples.

Peraluminous tonalites have plagioclase + quartz + cordierite and/or sillimanite + garnet + orthopyroxene + muscovite + biotite. Minor chlorite occasionally replaces biotite. Quartz ranges in size up to 0·9 mm and plagioclase up to 1·9 mm, but is typically 0·6 mm. The other phases range down in size from 0·4 mm. Enclaves of graphitic migmatitic Nakanagawa metasedimentary rock are found in some areas (Fig. 3b). Graphite is relatively abundant in peraluminous tonalites compared with other intrusive phases, although is an accessory phase only (Fig. 4a and b). The other opaque phases include pyrrhotite, chalcopyrite, and ilmenite, with a combined abundance of ~1%.

Sulfide deposits within the OGC

The Horoman Mine exploited a massive to disseminated sulfide body hosted in the gabbronorite unit, and mineralized rocks associated with this deposit crop out near the eastern fringes of the OGC. This mine stopped operating in the 1950s, before a good understanding of magmatic sulfide ore genesis had been developed, and appears to have been a relatively small operation. Minor sulfide mineralization also occurs in the south of the eastern OGC in the Pon-Nikambetsu valley.

The Horoman Mine sulfide mineralization consists of disseminated to massive pyrrhotite + chalcopyrite + pentlandite ± cobaltite. Ilmenite is common, magnetite is rare, and graphite is observed in some outcrops (see also Funahashi & Igi, 1956). In massive sulfides, graphite is dominantly located within micro-enclaves of silicate material (Fig. 5a). However, rare rosettes of graphite are observed within massive sulfide (Fig. 5b). This latter observation implies that a trace fraction of graphite was dissolved in the sulfide melt, which is consistent with the experimentally observed low solubility of carbon in pyrrhotite and pentlandite melts (Palyanov *et al.*, 2006). Silicate inclusions in the massive sulfide can be rounded, in which case they are commonly rimmed by magnetite ± ilmenite ± graphite (Fig. 5c), or angular. Oxide mineral inclusions in the massive sulfide are dominantly ilmenite and are typically well rounded. Pentlandite is relatively minor in the massive and disseminated sulfide, and chalcopyrite is generally more abundant. Chalcopyrite tends to be hosted in fractures that transect silicate enclaves in massive sulfide, or in veinlets in semi-massive sulfide. Disseminated sulfide typically coexists with sparse graphite (e.g. Fig 5d).

The Pon-Nikambetsu valley mineralization is similar to the Horoman deposit and consists of pyrrhotite + chalcopyrite + pentlandite + ilmenite, although Funahashi & Igi (1956) found a higher proportion of chalcopyrite here than in the Horoman sulfides. Elsewhere in the OGC, small sub-spherical sulfide globules (up to 0·5 mm) are common, and are typically associated with biotite-rich intermediate intrusive rocks.

Nakanogawa Group metasediments

The OGC is bounded to the west and south primarily by gneisses, mylonites, and migmatites of the metasedimentary Nakanogawa Group, and to the east by peraluminous tonalites (Fig. 2). The Nakanogawa Group is part of the Hidaka Supergroup, a latest Cretaceous to Early Paleocene (Kiminami *et al.*, 1992) accretionary wedge complex. The Nakanogawa Group itself is mainly a succession of Paleocene turbidites sourced from both the paleo-Kuril Arc and the paleo-Japan Arc margins (Nanayama *et al.*, 1993). Detrital clinopyroxene grains in the sediments of the southern and central parts of the Nakanogawa Group reflect the input of nearby calc-alkaline and tholeiitic volcanism; two populations of chrome spinel grains occur throughout the entire Nakanogawa stratigraphy, originating from upper mantle peridotite and from an unconfirmed paleo-Kuril fore-arc ophiolite sequence (Nanayama *et al.*, 1993).

The Nakanogawa Group envelope immediately to the south of the OGC (Fig. 2) is incised by the Pon-Nikambetsu River, where it contains locally extensive areas of migmatization. Bodies of gabbro are present in the Pon-Nikambetsu River section and are, in one locality, associated with a small massive sulfide occurrence. The migmatites in this area contain abundant graphite confined mostly to biotite-rich melanosomes. Leucosomes within the migmatite have andalusite porphyroblasts and lack any peritectic porphyroblasts, indicating that melting took place under water-saturated conditions at this locality. In other localities, such as in the Tottabetsu River to the north (see Kamiyama *et al.*, 2007), migmatites

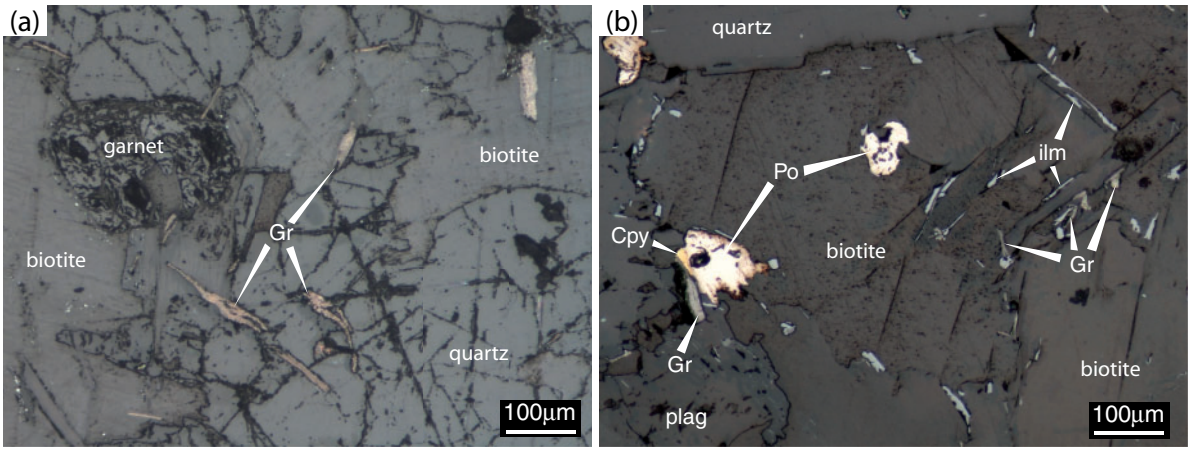

Fig. 4. Reflected light photomicrographs of the peraluminous tonalite. (a) Abundant graphite flakes amongst quartz, biotite and garnet. (b) Sulfides, graphite and ilmenite amongst biotite, quartz and plagioclase. Gr, graphite; Po, pyrrhotite; Cpy, chalcopyrite; ilm, ilmenite; plag, plagioclase.

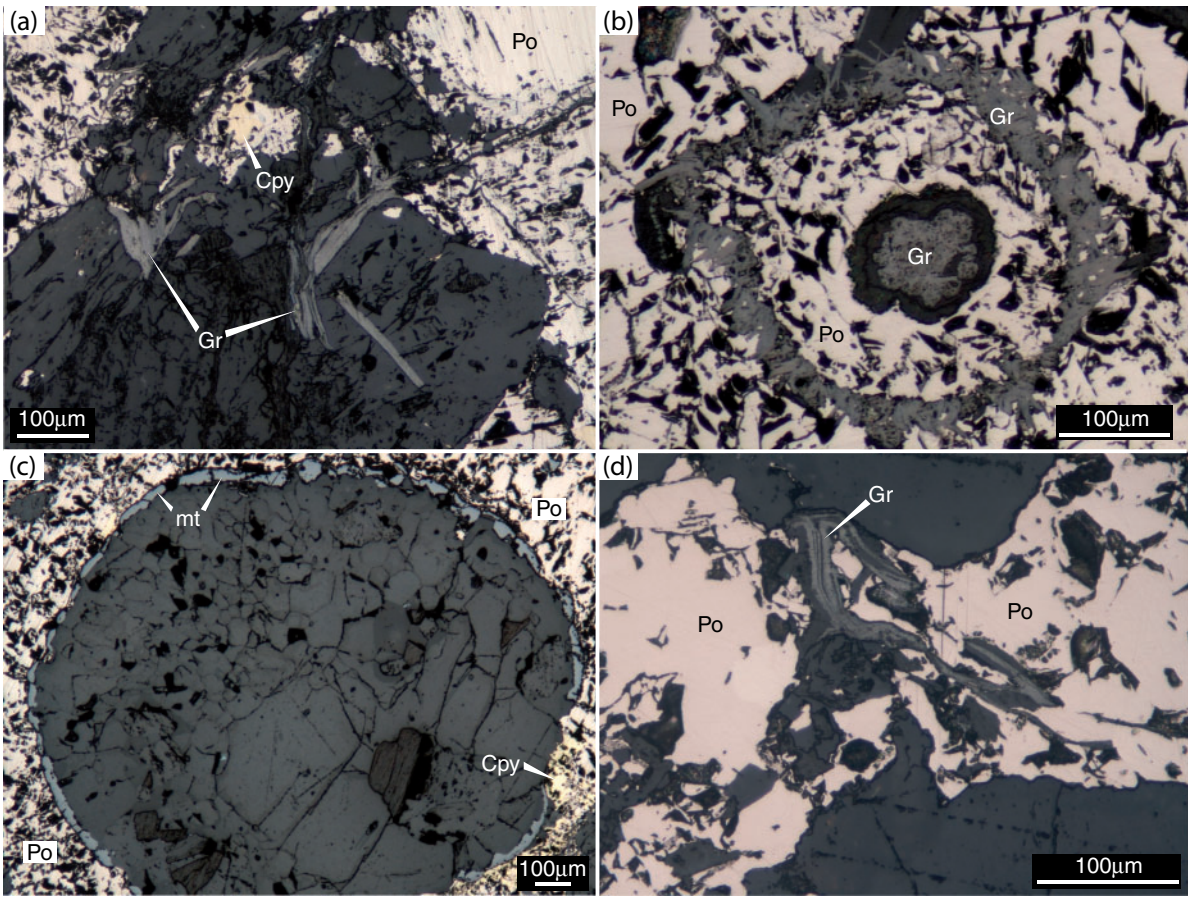

Fig. 5. Reflected light photomicrographs that illustrate the textural relationships in sulfide-rich samples at the Horoman Mine. (a) Graphite in a silicate inclusion in massive sulfide. (b) A graphite rosette in massive sulfide, showing randomly oriented crystalline graphite. (c) A spherical silicate inclusion in massive sulfide with magnetite rim. (d) Graphite associated with disseminated pyrrhotite. Gr, graphite; Po, pyrrhotite; Cpy, chalcopyrite; mt, magnetite.

containing peritectic garnet and orthopyroxene have been found, indicating that in some areas the Nakanogawa Group underwent high-temperature dehydration melting of the type that produces tonalitic melt (e.g. Shimura *et al.*, 1991). Moreover, amphibolites in the SW and NW edges of the OGC are observed to have undergone some minor dehydration melting, consistent with high-temperature metamorphism in the lower parts of the sequence. Shiba & Morinaga (1998) conducted a detailed structural examination of the shear movement associated with mylonite development in the Nakanogawa Group around the OGC, and found that SE-directed movement of the complex occurred under lower granulite- to amphibolite-facies metamorphic grade. Mylonitization is concentrated in the biotite gneiss and peraluminous tonalite that surrounds the OGC.

Sample selection

The 40 samples on which various geochemical analyses were performed are listed in Table 1. We also examined a further 25 thin sections and 19 polished mounts from additional samples as part of this study. All samples were collected during a period of field work in 2006, from outcrops along creeks and rivers that transect the OGC and surrounding region. Vegetation in the area is dense and the topography is mountainous, and these sampling locations represent the only efficiently accessible areas of abundant outcrop. The main transect of samples was collected along a creek that crosses mineralized rocks surrounding the abandoned Horoman Ni–(Cu) mine; other samples come from the larger region (Fig. 2). Sample selection in the field was carried out on the basis of lack of weathering, and with the aim of collecting a representative range of the rocks types observed. Sample selection for geochemical analysis was done after observation of thin sections, again aiming to represent the range of rocks observed.

Analytical methods

All analyses for major and trace elements were made on whole-rock powders. Platinum group element (PGE), S isotope and C isotope data were collected on whole-rock powders and sulfide separates as indicated in Tables 2–7. Samples were milled to powders in a tungsten carbide mill for X-ray fluorescence (XRF) major element analysis and in a zirconia mill for inductively coupled plasma mass spectrometry–atomic emission spectrometry (ICPMS-AES) trace element analysis. Samples for PGE analyses were milled to powders in zirconia or agate. Sulfide separates for PGE analyses and S isotopes were prepared by milling in agate followed by sieving for the desired size fraction ($180\,\mu m < \sigma < 220\,\mu m$).

Analyses for major elements were carried out by XRF on lithium metaborate fusion-discs at the James Cook University Advanced Analytical Centre (JCU-AAC) on whole-rock powders. For trace elements, combined nitric, perchloric, and hydrofluoric acid sealed-bomb microwave-oven digestion was used to prepare whole-rock powders for analysis by ICPMS-AES. Analyses were performed using a Varian Liberty Series II ICP-MS system housed at the JCU-AAC. Indium was used as an internal standard to check for instrument drift during analysis.

Total sulfur analysis was performed by IR spectroscopy at GeoLabs. Each sample was combusted in an oxygen-rich environment to oxidize the sulfur in the sample matrix. The vaporized sulfur-containing stream was then analysed by IR absorption.

PGE analyses were performed by the nickel sulfide fire assay method at Geolabs in Ontario, Canada. Whole-rock and sulfide separate powders were fused with a nickel and sulfur mixture to produce a sulfide button. This button was then dissolved in acid followed by coprecipitation with Te, producing a PGE concentrate containing Ru, Rh, Pd, Pt, Ir, and Au tellurides. The concentrate was dissolved in aqua regia prior to analysis by ICP-MS. These data are reported in Electronic Appendix 1 (available for downloading at http://www.petrology.oxfordjournals.org).

Sulfur isotope data were obtained using a Finnigan MAT elemental analyser–continuous flow isotope ratio mass spectrometer at Monash University. For sulfur isotopes, whole-rock powders were combined with ~0·5 g of VO_5 in SnO_2 cups and combusted in an oxidizing furnace column at 950°C. Standards were included preceding and following each sample run to allow for calibration and drift correction.

Carbon isotope ratios were measured following procedures outlined by Clark & Fritz (1997) at the Monash University School of Geosciences. The samples were washed with a dilute solution of ~1% HCl, afterwards washed several times with ultrapure water solution and then put in an oven to dry overnight. Samples were then loaded in tin cups and combusted to CO_2 using a Carlo Erba 1110 Flash Elemental Analyser coupled with a Thermo Delta Plus Advantage Mass Spectrometer. $\delta^{13}C$ values were measured by continuous flow. Standardization of $\delta^{13}C$ to the CDT scale was via analysis of the USGS 24 graphite standard.

GEOCHEMISTRY OF THE OGC

Major elements

Major element variation diagrams have been used to classify the intrusive rocks of the OGC; these are slightly more calcic than calc-alkaline, dominantly low-K series and low-Fe series (Fig. 6; Table 2), following the approach of Arculus (2003). Harker variation diagrams of major element oxides against SiO_2 for this suite are consistent with fractionation trends typical of subalkaline arc magmas (Figs 6 and 7). This is shown by elevated Al_2O_3 and increasing K_2O and FeO*/MgO with increasing

Table 1: Location and basic description of studied rock samples

Rock ID	Rock type	Mineralogy	Latitude	Longitude
KR003	Sulfide-rich gabbro	Altered ol, px, pl; abund. po; minor cpy, graphite; trace ilm, gers, pnt	42°8′41·1″	143°10′23·6″
KR005	Massive sulfide	Abund. po; minor cpy, ilm; trace gers, graphite, pnt	42°8′41·1″	143°10′23·6″
KR013	Massive sulfide	Abund. po; minor cpy, ilm; trace gers, graphite, pnt	42°8′41·5″	143°10′32·6″
KR015	Sulfide-rich gabbro	Altered ol, px, pl; abund. po; minor cpy, graphite; trace gers, pnt	42°8′46·4″	143°10′35·5″
KR030A	Medium-grained cumulate olivine gabbro	ol, pl, opx; minor po, cpy	42°9′35·7″	143°7′5·6″
KR061	Gabbro with abund. disseminated sulfides	Abund. px, pl; minor bt, amph; po, cpy, ilm	42°6′7·2″	143°8′48·4″
KR044.1	Gabbro with abund. disseminated sulfides	Abund. px, pl; minor bt, amph; abund. po, cpy; minor ilm	42°6′55·8″	143°9′40″
KR044.3	Sulfide-bearing gabbro	Abund. px, pl; minor bt, amph; abund. po, cpy; minor ilm	42°6′55·8″	143°9′40″
KR049	Coarse-grained gabbro	pl, px, ol; minor po, cpy, pnt, ilm	42°6′5·6″	143°8′40·1″
KR006	Coarse-grained gabbro with pegmatoid	Ol, pl, cpx, amph; minor ilm; trace po	42°8′40·1″	143°10′8·2″
KR043.3	Fine- to coarse-grained gabbro	px (altered), amph, bt, pl, qz; po, cpy	42°7′1·9″	143°9′30·7″
KR039	Gabbro	px, pl, amph, bt–no ol; diss. ilm	42°7′6″	143°9′20·8″
KR023	Coarse gabbro–diorite	px, pl, amph; minor sulfide	42°9′1·3″	143°10′22″
KR002	Gabbro–diorite with sulfide spots	px, pl, amph, bt; minor po, cpy	42°8′41″	143°10′19″
KR092.2	Gabbro–diorite	px, pl, amph, bt; minor po, cpy	42°8′37·4″	143°9′56·0″
KR028	Fine-grained gabbro–diorite	px, pl, bt; minor ilm	42°8′34·6″	143°9′1″
KR008	Medium- to fine-grained gabbro–diorite	60/40 pl/cpx	42°8′39·4″	143°10′12·7″
KR025.1	Medium-grained gabbro–diorite	px, amph, bt, pl; minor po; trace cpy	42°8′3·4″	143°9′50·5″
KR043.1	Fine-grained gabbro–diorite (from mingled outcrop, KR43.1 mingled with KR43.2)	px, pl, bt, ksp; no qtz; diss po	42°7′1·9″	143°9′30·7″
KR046.1	Medium- to coarse-grained gabbro–diorite	pl, amph, bt, cpx; diss ilm in bt; minor po, cpy	42°6′50·5″	143°10′4·5″
KR045.1	Gabbro–diorite	Amph, bt, pl, minor qz; diss ilm, minor po, cpy	42°6′55·1″	143°9′53″
KR045.2	Gabbro–diorite	Amph, bt, pl, minor qz; diss ilm, minor po, cpy	42°6′55·1″	143°9′53″
KR019	Gabbro–diorite	Amph, pl, qz, + chl pseudomorphing bt; minor ilm, po; trace cpy, graphite	42°8′36·6″	143°10′43·2″
KR017	Diorite	bt, amph, pl, qz, kfs; minor ilm; trace po, cpy, graphite	42°8′39·3″	143°10′39·9″
KR018	Diorite	pl, amph, alt bt, qz; minor ilm; trace po, cpy, graphite	50 m upstream from KR017	
KR062	Diorite with sulfide	pl, amph, bt, qz; diss po, cpy ilm; trace graphite	42°6′33″	143°8′52·8″
KR060.2	Diorite (sampled adjacent to contact with tonalite)	pl, amph, bt, qz; trace po, cpy ilm	42°6′4·5″	143°8′38·9″
KR047	Coarse-grained diorite	bt, amph, pl, qtz; minor diss. ilm, po, cpy, graphite	42°7′1·3″	143°9′6·9″
KR057.2	Sheared diorite	bt, amph, pl, qtz; minor ilm	42°9′8·8″	143°4′59·5″
HID12a	Peraluminous tonalite	Pl, qtz, bt, msc, grt, crd, opx; widespread minor graphite	42°5′24·8″	143°10′26·4″
HID12c	Peraluminous tonalite	Pl, qtz, bt, msc, sill, crd, grt; widespread minor graphite; trace po, cpy	42°5′24·8″	143°10′26·4″

(continued)

Table 1: Continued

Rock ID	Rock type	Mineralogy	Latitude	Longitude
KR071	Peraluminous tonalite (outcrop contains many enclaves; foliated)	Pl, qtz, bt, crd; minor diss po, cpy	42°5′24·8″	143°10′26·4″
KR097	Peraluminous tonalite (foliated)	Pl, qtz, bt, crd; minor diss po, cpy	42°5′28·0″	143°10′27·1″
KR024	Peraluminous tonalite	Qtz, pl, bt; widespread minor po, cpy; trace graphite	42°8′23·2″	143°9′35·5″
KR025.2	Metaluminous tonalite	Pl, qtz, bt; minor diss po, cpy		
KR031	Metaluminous tonalite	Pl, qtz, bt, amph; no sulfides	42°9′25·6″	143°5 39·1″
KR026	Metaluminous tonalite	Qtz, pl, bt, resorbed amph; widespread minor po, cpy; trace graphite	42°8′12·9″	143°10′14·2″
KR037.2	Metaluminous tonalite (enclaves)	Pl, qtz, bt; minor diss po, cpy	42°6′2·7″	143°8′22″
KR027.2	Coarse tonalite	Coarse pl, qz, bt	42°8′26·7″	143°9′48·7″
KR060.1	Leucogranite	Qtz, ksp, pl; minor bt		
KR091.2	Leucogranite	Qtz, ksp, pl; minor bt	42°8′38·1″	143°9′56·0″
KR007	Leucogranite	Qtz, microcline, pl; minor bt	42°8′40·1″	143°10′9·8″
KR020	Carbonaceous metasediment (multiply deformed)	Qtz, pl, chl, grt, diss po, cpy; trace graphite	42°8′34·2″	143°10′54·3″
KR021	Carbonaceous metasediment (foliated)	Qtz, pl, bt; minor graphite, po, cpy	42°8′35·3″	143°10′57″
KR036	Migmatite	Qtz, pl, bt, ms	42°7′55·8″	143°6′13·1″
OS1	Migmatite with chiastolite porphyroblasts; oriented sample	Qtz, pl, bt, ms, and	42°6′1·8″	143°8′23·5″
KR037.1	Migmatite	Qtz, pl, bt, ksp; widespread po; trace cpy		
KR050	Andalusite-bearing migmatite	Qtz, bt, pl, ms, ksp, and; widespread po; trace cpy; graphite in some layers	42°5′53·9″	143°7′53·4″
KR035.2	Migmatite	Qtz, bt, pl, msc, ksp, crd, sill; trace graphite, po, cpy	42°8′4·5″	143°6′12·6″

SiO_2. The cumulate troctolite gabbro has the lowest SiO_2 content at 43 wt %. Its cumulate nature accounts for the elevated MgO content; it is also depleted in Na_2O, P_2O_5, CaO, Al_2O_3, and TiO_2 compared with the rest of the OGC suite. The increasing Na_2O, K_2O and P_2O_5, and decreasing CaO, Fe_2O_3, MgO, and MnO contents with increasing SiO_2 are characteristics of subalkaline arc magma differentiation trends. These trends imply fractionation of olivine, pyroxene, hornblende and calcic plagioclase from the OGC magmas.

The tonalites studied here can be subdivided into two groups based on their alumina saturation index (ASI). Some tonalites are distinctly peraluminous with ASI values between 1·29 and 1·5 (samples HID12a, HID12c, KR071, KR097); others are metaluminous to slightly peraluminous with ASI values between 0·97 and 1·1 (samples KR025.2, KR031, KR026, KR037.2). For the ease of subsequent discussion, these two groupings are referred to as peraluminous and metaluminous tonalites respectively. There is one intermediate sample (KR024) with an ASI value of 1·17, which we place into the peraluminous group. All samples with bulk $SiO_2 > 70$ wt % are from late-stage leucogranite dikes that cut across the other igneous rocks.

Trace elements

Field evidence suggests that magma mixing may have been an important process in the overall petrogenetic development of the igneous suite. If this is the case, then the curvilinear trends in many of the major element variation diagrams between mafic (~49 wt % SiO_2) and felsic (~65 wt % SiO_2) end-members, consistent with fractional crystallization, obscure the role of mixing. Figure 8 shows the trace element patterns (data in Table 2), normalized to average normal (N)-MORB, of two of the most primitive gabbros in our sample suite that were collected in the vicinity of the Horoman Mine, one of which has been used in the assimilation–fractional crystallization (AFC) modelling described below. The rare earth element (REE) profiles are flat and depleted relative to N-MORB, and are similar to those of primitive arc basalts in the Vanuatu

Table 2: Whole-rock XRF data

Sample:	KR061	KR044.1	KR049	KR002	KR092.2	KR028	KR008	KR025.1	KR043.1	KR046.1	KR045.2
Rock type:	Gabbro	Gabbro	Gabbro	Gabbro-diorite	Gabbro-diorite	Gabbro-diorite	Gabbro-diorite	Gabbro-diorite	Gabbro-diorite	Gabbro-diorite	Gabbro-diorite
SiO_2	47·5	48·0	48·1	52·5	53·4	53·8	53·8	54·0	54·2	54·3	54·5
TiO_2	0·58	0·78	0·80	1·18	0·83	1·15	1·01	1·15	0·97	0·93	0·95
Al_2O_3	19·2	14·5	21·3	15·9	16·8	16·8	15·5	16·2	16·6	17·7	16·6
Fe_2O_3	7·01	15·2	6·74	9·08	6·99	7·89	8·64	8·71	7·48	6·81	7·85
MnO	0·11	0·17	0·11	0·15	0·13	0·15	0·17	0·14	0·13	0·13	0·15
MgO	10·6	6·73	9·72	6·87	7·58	6·63	7·64	6·10	6·90	7·07	6·77
CaO	9·72	8·44	10·8	9·09	9·72	9·64	9·84	8·58	9·10	9·36	6·38
Na_2O	2·13	2·57	2·31	2·53	2·80	2·90	3·02	2·64	2·97	2·45	3·58
K_2O	0·45	0·36	0·05	0·92	0·72	0·32	0·26	1·71	0·91	0·82	1·53
P_2O_5	0·07	0·09	0·07	0·11	0·10	0·16	0·10	0·15	0·11	0·11	0·12
SO_3	b.d.	0·07	b.d.	b.d.	b.d.	b.d.	b.d.	b.d.	b.d.	b.d.	b.d.
LOI	2·66	2·11	0·29	2·00	1·08	1·07	0·99	0·78	1·05	1·04	2·01
Total	99·9	99·0	100·2	100·3	100·1	100·5	101·0	100·1	100·4	100·7	100·4
Ce	6·51	14·5	6·15	15·8	16·9	21·0	13·1	29·9	22·1	17·6	22·2
Dy	2·09	3·52	2·63	4·22	3·89	5·19	4·27	5·44	4·59	3·60	4·22
Er	1·25	2·10	1·60	2·60	2·39	3·09	2·65	3·20	2·77	2·18	2·51
Eu	0·784	1·12	0·795	1·26	1·01	1·31	1·06	1·33	1·14	0·971	1·08
Gd	1·91	3·16	2·39	3·67	3·47	4·73	3·71	5·00	4·21	3·36	3·95
Ho	0·425	0·702	0·532	0·842	0·789	1·03	0·872	1·07	0·907	0·724	0·853
La	2·39	5·83	1·81	6·33	7·01	8·17	4·99	12·6	8·97	7·69	9·31
Lu	0·176	0·311	0·227	0·376	0·343	0·428	0·382	0·460	0·395	0·317	0·360
Nd	5·09	9·49	5·83	10·5	10·4	14·4	9·71	17·5	13·3	10·6	12·9
Pr	1·00	2·04	1·07	2·20	2·33	3·03	1·95	3·95	2·95	2·36	2·95
Sc	20·8	35·2	18·3	37·6	40·3	41·0	42·6	43·6	39·5	32·7	38·9
Sm	1·58	2·76	1·92	3·12	3·00	4·18	3·05	4·67	3·68	2·94	3·52
Tb	0·326	0·550	0·401	0·643	0·614	0·827	0·643	0·846	0·711	0·561	0·655
Tm	0·174	0·288	0·218	0·348	0·329	0·422	0·360	0·443	0·378	0·301	0·349
Y	12·4	20·1	15·5	23·1	23·5	29·9	24·6	31·0	27·2	21·4	24·9
Yb	1·22	2·04	1·55	2·54	2·32	2·93	2·57	3·07	2·71	2·15	2·44
Ag	0·139	2·69	0·143	0·0564	0·119	0·190	0·109	0·264	0·0925	0·320	0·112
As	1·37	3·03	<1	0·985	5·99	1·90	0·762	4·86	8·89	2·54	31·2
Ba	52·8	97·5	5·77	191	106	72·7	63·7	292	216	138	277
Bi	<0·05	2·20	<0·05	<0·05	<0·05	<0·05	<0·05	<0·05	<0·05	<0·05	<0·05
Cd	0·204	1·38	0·110	0·0952	0·117	0·154	0·120	0·170	0·110	0·137	0·147
Co	88·7	320	81·0	37·5	57·1	53·0	47·5	49·8	55·0	50·8	63·0
Cr	257	613	110	202	880	442	284	505	644	60·5	59·7
Cu	107	8·60	101	32·1	73·5	44·0	4·78	43·2	29·8	616	592
Ga	13·9	15·2	14·1	15·7	17·7	17·1	13·3	23·7	20·8	17·4	22·0
Ge	3·04	4·91	3·06	3·60	3·99	4·18	3·84	4·62	4·17	3·32	4·07
Hf	1·42	1·34	2·03	1·24	1·79	2·54	2·13	3·33	1·26	3·65	1·06
Mn	630	896	867	994	<43·1	973	1050	923	346	993	776
Mo	<0·1	<0·1	<0·1	<0·1	<0·1	<0·1	<0·1	<0·1	<0·1	<0·1	<0·1
Nb	1·84	2·35	1·29	3·43	3·14	4·32	2·48	5·96	4·08	3·41	4·41
Ni	262	2660	334	27·8	144	79·5	61·5	55·3	97·9	117	147
Pb	2·56	14·1	0·151	3·45	5·27	3·22	3·78	7·11	5·36	2·87	5·33
Rb	10·7	5·52	0·538	22·3	16·8	5·26	3·50	49·0	21·0	19·3	41·0
Sb	<0·05	<0·05	<0·05	0·137	<0·05	<0·05	<0·05	<0·05	<0·05	<0·05	<0·05
Se	4·92	8·76	5·05	2·53	5·92	5·55	3·34	5·13	5·09	5·03	4·98

(continued)

Table 2: Continued

Sample:	KR061	KR044.1	KR049	KR002	KR092.2	KR028	KR008	KR025.1	KR043.1	KR046.1	KR045.2
Rock type:	Gabbro	Gabbro	Gabbro	Gabbro–diorite	Gabbro–diorite	Gabbro–diorite	Gabbro–diorite	Gabbro–diorite	Gabbro–diorite	Gabbro–diorite	Gabbro–diorite
Sn	1·05	0·971	0·627	0·666	3·44	0·795	1·48	1·21	1·28	1·18	2·50
Sr	274	197	230	264	219	239	321	272	265	206	265
Ta	0·172	0·180	0·147	0·388	0·224	0·268	0·272	0·434	0·302	0·248	0·352
Te	0·610	0·898	0·256	0·339	0·589	<0·05	0·192	<0·05	0·313	0·319	0·277
Ti	5230	5750	7910	6910	2480	3990	6220	6750	4150	5410	4620
Tl	<0·05	<0·05	<0·05	0·112	0·0924	<0·05	<0·05	0·251	0·114	0·102	0·189
W	<0·1	2·62	0·664	1·27	3·82	1·67	1·42	9·45	6·73	0·119	0·802
Zn	90·0	178	73·6	100·0	99·3	105	87·0	133	102	84·6	114

Sample:	KR027.1	KR045.1	KR019	KR018	KR062	KR060.2	KR047	KR057.2	KR097	KR024	KR025.2
Rock type:	Gabbro–diorite	Gabbro–diorite	Gabbro–diorite	Diorite	Diorite	Diorite	Diorite	Diorite	Peralum. tonalite	Peralum. tonalite	Metalum. tonalite
SiO_2	55·3	56·7	56·8	58·5	58·8	59·4	60·0	61·8	64·7	65·7	63·7
TiO_2	0·54	0·84	0·71	1·26	1·09	0·96	1·19	0·40	0·69	0·92	0·84
Al_2O_3	16·4	16·9	16·9	16·0	17·6	16·7	17·1	18·3	16·6	15·8	16·0
Fe_2O_3	6·49	7·45	6·97	8·11	5·93	8·49	8·03	4·59	5·79	5·89	6·18
MnO	0·11	0·13	0·13	0·14	0·10	0·12	0·13	0·10	0·07	0·08	0·08
MgO	7·69	6·41	6·19	4·24	4·55	3·83	3·60	3·71	2·31	2·40	3·07
CaO	9·27	7·43	7·24	6·26	6·76	4·47	5·29	5·82	2·34	3·00	3·81
Na_2O	2·77	2·57	2·38	3·30	3·21	2·90	3·45	3·98	2·75	3·26	3·62
K_2O	0·73	0·72	1·16	0·89	1·37	1·82	1·07	0·72	2·80	2·52	1·91
P_2O_5	0·06	0·12	0·10	0·19	0·14	0·07	0·19	0·07	0·16	0·20	0·11
SO_3	b.d.	b.d.	b.d.	b.d.	b.d.	b.d.	b.d.	b.d.	b.d.	b.d.	0·03
LOI	0·90	0·94	1·98	1·18	0·74	1·07	0·64	1·32	1·47	0·70	1·23
Total	100·2	100·2	100·6	100·0	100·3	99·8	100·7	100·8	99·7	100·5	100·7
Ce	19·5	25·3	27·3	30·1	30·4	37·6	35·2	21·4	51·5	41·7	25·3
Dy	3·66	4·16	3·40	5·23	4·37	2·53	3·45	3·03	1·83	1·72	1·42
Er	2·14	2·54	1·97	3·16	2·48	1·63	2·12	1·85	0·612	0·570	0·843
Eu	0·871	1·24	1·19	1·24	1·30	1·51	1·65	0·857	1·03	0·882	1·18
Gd	3·32	3·96	3·42	4·90	4·28	2·70	3·86	2·87	3·58	3·08	1·87
Ho	0·726	0·834	0·667	1·05	0·847	0·507	0·708	0·605	0·280	0·247	0·288
La	8·18	11·0	12·2	12·5	12·5	18·0	16·3	9·41	23·4	18·0	13·1
Lu	0·305	0·380	0·284	0·469	0·328	0·277	0·354	0·293	0·0636	0·0617	0·147
Nd	11·2	14·1	14·1	17·5	16·3	15·6	17·0	11·1	23·2	19·3	10·5
Pr	2·58	3·24	3·38	3·94	3·80	4·04	4·15	2·66	6·15	4·86	2·73
Sc	37·2	36·0	31·0	29·9	26·6	32·1	30·3	19·2	21·0	17·5	27·4
Sm	3·13	3·70	3·41	4·58	4·12	3·01	3·87	2·79	4·74	4·02	1·95
Tb	0·576	0·654	0·551	0·819	0·711	0·417	0·572	0·481	0·445	0·390	0·258
Tm	0·300	0·354	0·271	0·442	0·333	0·237	0·311	0·266	0·0740	0·0681	0·127
Y	20·7	24·4	19·2	29·9	25·3	14·9	20·4	18·2	6·83	6·34	8·64
Yb	2·06	2·55	1·91	3·13	2·30	1·83	2·28	1·91	0·484	0·468	0·912
Ag	0·198	0·268	0·188	0·214	0·239	0·224	0·154	0·195	0·261	0·346	0·258
As	3·33	6·81	2·49	1·24	1·83	<1	4·23	<1	1·58	<1	<1
Ba	185	255	220	183	274	443	311	223	277	592	546
Bi	<0·05	<0·05	<0·05	<0·05	<0·05	<0·05	<0·05	0·291	<0·05	0·0850	<0·05

(continued)

Table 2: Continued

Sample:	KR027.1	KR045.1	KR019	KR018	KR062	KR060.2	KR047	KR057.2	KR097	KR024	KR025.2
Rock type:	Gabbro-diorite	Gabbro-diorite	Gabbro-diorite	Diorite	Diorite	Diorite	Diorite	Diorite	Peralum. tonalite	Peralum. tonalite	Metalum. tonalite
Cd	0·274	0·182	0·182	0·155	0·132	0·110	0·125	0·100	0·138	0·148	0·0992
Co	64·5	48·9	43·7	29·0	33·2	45·2	39·8	27·3	21·5	26·9	27·6
Cr	662	576	284	134	295	343	244	107	139	158	162
Cu	142	23·2	39·9	26·5	31·9	127	73·7	13·5	17·5	66·7	76·1
Ga	17·5	21·5	18·9	18·2	25·1	30·2	26·7	21·8	23·0	34·7	33·2
Ge	3·61	3·93	3·68	3·84	3·90	4·75	4·39	3·18	3·44	4·73	4·58
Hf	2·53	3·35	2·43	3·52	3·22	1·70	1·50	1·83	3·52	3·44	2·40
Mn	185	986	766	862	598	500	584	312	943	507	798
Mo	<0·1	<0·1	<0·1	<0·1	<0·1	<0·1	<0·1	<0·1	<0·1	<0·1	<0·1
Nb	2·54	4·88	4·77	6·31	7·06	9·18	10·2	2·79	4·22	10·9	10·2
Ni	357	86·9	96·3	29·5	29·9	159	87·0	76·0	45·3	66·6	72·5
Pb	7·04	5·78	18·0	4·97	6·91	9·08	8·41	7·49	9·39	14·1	13·9
Rb	17·1	10·5	36·1	23·6	37·7	44·7	23·1	13·2	32·2	76·8	59·1
Sb	<0·05	<0·05	<0·05	<0·05	<0·05	<0·05	<0·05	<0·05	<0·05	<0·05	<0·05
Se	4·23	4·10	3·59	3·70	5·32	4·95	4·24	4·42	5·09	4·89	6·09
Sn	0·721	0·419	1·70	1·18	2·06	1·06	0·953	1·90	1·56	2·20	2·00
Sr	230	275	274	240	251	445	384	364	293	332	268
Ta	0·272	0·339	0·395	0·447	0·539	0·576	0·678	0·257	0·331	0·804	0·680
Te	0·128	0·374	0·329	0·274	0·325	0·264	0·253	0·129	0·155	<0·05	<0·05
Ti	3010	4040	4370	7280	3070	2030	4010	5800	6920	5930	4240
Tl	0·0769	0·0692	0·166	0·130	0·203	0·255	0·130	0·0769	0·191	0·405	0·372
W	4·44	1·45	3·27	2·03	0·981	2·15	≤0·1	1·73	4·11	1·32	2·53
Zn	84·5	122	103	121	96·2	165	150	67·4	78·8	147	146

Sample:	KR031	KR037.2	KR091.2	KR021	KR020	KR036	OS1	KR037.1	KR050	KR035.2
Rock type:	Metalum. tonalite	Metalum. tonalite	Leuco-granite	Carb. metased.	Carb. metased.	Migmatite	Migmatite	Migmatite	Migmatite	Migmatite
SiO_2	64·2	68·1	76·8	62·5	64·9	63·1	63·2	65·0	65·4	69·6
TiO_2	0·48	0·69	0·43	0·72	0·68	0·80	0·87	0·69	0·73	0·53
Al_2O_3	17·2	16·1	12·3	18·0	16·3	17·9	17·2	15·9	16·1	14·4
Fe_2O_3	4·16	3·87	1·05	5·78	5·99	5·63	7·31	5·69	6·03	4·50
MnO	0·09	0·06	0·01	0·11	0·27	0·09	0·08	0·07	0·06	0·06
MgO	3·05	1·48	0·29	2·44	2·43	2·46	2·71	2·34	2·17	2·33
CaO	5·55	3·57	0·85	2·75	2·38	2·60	2·46	3·53	2·34	3·32
Na_2O	3·63	3·39	1·84	2·89	2·66	3·23	2·25	2·98	2·45	3·51
K_2O	1·53	2·40	5·92	3·30	2·90	2·84	2·38	2·17	2·88	1·04
P_2O_5	0·09	0·15	0·05	0·09	0·11	0·15	0·16	0·15	0·19	0·09
SO_3	b.d.	b.d.		0·02	0·01	b.d.	b.d.	b.d.	b.d.	b.d.
LOI	0·71	0·62	0·30	2·35	1·95	1·74	1·39	1·19	1·63	0·56
Total	100·6	100·4	99·8	100·9	100·6	100·6	100·0	99·7	100·0	99·9
Ce	52·8	32·8	14·3	74·6	58·0	52·4	44·5	47·2	44·1	29·9
Dy	3·42	3·93	0·946	1·97	3·84	1·92	2·21	2·42	2·03	2·45
Er	1·71	2·10	0·461	0·945	2·48	0·609	0·852	1·08	0·753	1·40
Eu	1·08	0·915	0·759	1·06	1·08	1·08	1·21	1·06	0·997	0·971
Gd	4·67	3·84	1·29	3·75	4·28	3·49	3·46	3·36	3·25	2·68
Ho	0·651	0·726	0·174	0·347	0·755	0·270	0·346	0·415	0·318	0·465

(continued)

Table 2: Continued

Sample:	KR031	KR037.2	KR091.2	KR021	KR020	KR036	OS1	KR037.1	KR050	KR035.2
Rock type:	Metalum. tonalite	Metalum. tonalite	Leuco-granite	Carb. metased.	Carb. metased.	Migmatite	Migmatite	Migmatite	Migmatite	Migmatite
La	24·7	13·1	6·52	33·3	25·5	23·1	20·5	22·3	20·0	13·4
Lu	0·204	0·260	0·0444	0·126	0·514	0·0481	0·0840	0·117	0·0747	0·232
Nd	24·2	15·7	6·74	32·1	25·8	23·1	21·0	20·7	19·4	13·6
Pr	6·05	3·84	1·63	8·48	6·65	5·98	5·32	5·43	5·03	3·54
Sc	23·9	13·4	3·78	17·4	17·3	22·7	25·7	20·5	19·2	15·7
Sm	4·80	3·98	1·41	5·58	5·27	4·69	4·33	4·22	4·06	3·07
Tb	0·639	0·645	0·178	0·440	0·648	0·443	0·465	0·473	0·436	0·427
Tm	0·229	0·275	0·0527	0·119	0·391	0·0637	0·0972	0·137	0·0864	0·209
Y	18·8	20·9	4·89	9·36	22·2	6·95	9·21	11·5	8·38	13·5
Yb	1·43	1·86	0·327	0·815	3·25	0·398	0·626	0·873	0·544	1·59
Ag	0·715	0·434	0·416	0·305	0·592	0·0887	0·0813	0·0794	0·102	0·244
As	4·52	<1	<1	0·729	1·55	1·72	<1	<1	<1	1·11
Ba	458	466	1640	720	631	377	454	370	420	263
Bi	<0·05	0·0590	<0·05	<0·05	<0·05	<0·05	<0·05	<0·05	0·0925	<0·05
Cd	0·224	0·174	0·0941	0·542	0·170	0·0729	0·0808	0·0987	0·0551	0·122
Co	24·9	13·2	3·98	27·4	33·1	12·4	31·6	31·9	23·5	22·2
Cr	181	62·4	14·9	133	132	248	366	446	281	281
Cu	48·0	20·8	9·24	61·5	111	51·7	76·0	101	55·4	32·1
Ga	29·3	29·5	54·7	35·4	31·5	30·7	31·1	26·6	28·1	21·7
Ge	4·33	3·36	1·98	3·95	4·09	4·68	5·30	4·61	4·46	3·44
Hf	8·94	5·58	5·27	3·25	5·48	<0·1	<0·1	<0·1	<0·1	3·00
Mn	484	349	112	623	1630	430	365	506	645	392
Mo	<0·1	<0·1	<0·1	<0·1	<0·1	<0·1	<0·1	<0·1	<0·1	<0·1
Nb	9·86	8·18	4·48	7·31	8·21	11·4	11·4	10·2	9·62	5·85
Ni	57·1	16·0	5·82	52·3	77·3	18·4	81·0	120	57·7	65·1
Pb	10·9	12·1	16·5	8·58	11·0	13·1	12·4	10·2	9·77	7·76
Rb	69·5	60·1	76·5	68·3	68·7	77·2	60·2	67·6	63·0	18·9
Sb	<0·05	<0·05	<0·05	<0·05	<0·05	<0·05	<0·05	<0·05	<0·05	<0·05
Se	4·66	4·45	4·66	3·98	4·13	4·98	5·54	5·14	4·93	4·26
Sn	1·40	2·85	0·0916	1·59	1·36	2·56	1·23	0·876	2·56	0·530
Sr	231	180	170	246	256	394	277	429	251	226
Ta	0·504	0·573	0·220	0·334	0·407	0·866	0·756	0·710	0·678	0·670
Te	<0·05	<0·05	<0·05	0·0809	0·169	<0·05	0·140	<0·05	<0·05	<0·05
Ti	5510	3510	6720	4060	3830	3620	3450	4500	3980	0·101
Tl	0·404	0·329	0·374	0·403	0·355	0·393	0·323	0·378	0·335	2040
W	1·68	0·299	<0·1	0·294	1·48	5·47	2·70	4·50	<0·1	0·926
Zn	119	91·7	17·7	155	115	151	166	118	129	85·1

Sample:	KR030A	KR006	KR044.3	KR039	KR023	KR011	KR043.2	KR017	HID12a	HID12c	KR071
Rock type:	Cum. gabbro	Gabbro	Gabbro	Gabbro	Gabbro–diorite	Gabbro–diorite	Gabbro–diorite	Diorite	Peralum. tonalite	Peralum. tonalite	Peralum. tonalite
SiO_2	43·2	49·4	50·6	51·4	52·3	56·4	56·4	57·7	63·5	63·5	64·3
TiO_2	0·07	0·44	0·75	0·73	0·61	0·68	1·23	0·92	0·76	0·81	0·73
Al_2O_3	12·0	17·6	17·4	20·2	14·6	15·8	16·9	17·0	17·0	16·7	16·7
Fe_2O_3	9·00	5·43	8·58	5·83	6·79	7·17	8·45	6·48	6·50	6·92	5·94

(continued)

Table 2: Continued

Sample:	KR030A	KR006	KR044.3	KR039	KR023	KR011	KR043.2	KR017	HID12a	HID12c	KR071
Rock type:	Cum. gabbro	Gabbro	Gabbro	Gabbro	Gabbro–diorite	Gabbro–diorite	Gabbro–diorite	Diorite	Peralum. tonalite	Peralum. tonalite	Peralum. tonalite
MnO	0·12	0·10	0·13	0·10	0·12	0·14	0·14	0·11	0·07	0·07	0·08
MgO	29·4	10·6	8·61	6·28	9·99	6·36	4·67	5·43	2·54	2·67	2·36
CaO	5·94	13·0	10·2	10·5	10·5	8·80	7·02	7·10	1·85	2·38	2·25
Na_2O	1·06	1·94	2·69	3·03	1·95	3·25	3·49	3·21	2·86	3·30	2·70
K_2O	0·03	0·30	0·29	0·59	1·92	0·95	1·36	1·07	3·02	2·96	2·97
P_2O_5	0·02	0·05	0·09	0·09	0·05	0·10	0·20	0·15	0·15	0·22	0·15
SO_3	0·02	0·01	0·04	0·01	0·01	0·02	0·02	0·01	0·01	0·02	b.d.
LOI	0·18	1·77	1·42	1·43	2·11	1·32	0·69	1·76	2·19	1·42	1·53
Total	100·9	100·7	100·8	100·1	100·0	101·0	100·6	100·9	100·4	100·9	99·7
Ce	0·411	3·64	12·3	12·0	4·95	18·8	30·6	27·2	32·5	41·3	50·4
Dy	0·123	1·65	3·31	3·19	2·68	4·09	5·61	4·27	1·53	2·01	3·63
Er	0·0840	1·03	2·01	1·96	1·65	2·40	3·24	2·53	0·558	0·687	1·85
Eu	0·133	0·661	0·848	0·796	0·632	0·974	1·40	1·03	0·774	0·916	1·04
Gd	0·120	1·46	3·05	2·98	2·33	3·99	5·69	4·32	2·51	3·57	4·40
Ho	0·0259	0·353	0·697	0·677	0·570	0·833	1·13	0·883	0·244	0·307	0·659
La	0·189	1·27	4·80	4·86	1·84	7·95	13·3	11·6	12·2	17·0	22·2
Lu	<0·0217	0·142	0·286	0·284	0·228	0·339	0·441	0·357	0·0595	0·0634	0·215
Nd	0·312	3·16	8·27	8·00	4·60	12·0	18·3	15·0	13·8	18·7	23·5
Pr	0·0620	0·598	1·74	1·70	0·837	2·57	4·06	3·45	3·44	4·66	5·94
Sc	11·0	46·8	47·9	36·5	66·3	51·2	47·9	35·0	25·2	26·2	19·7
Sm	0·0893	1·05	2·43	2·35	1·65	3·39	4·93	3·79	2·92	4·05	5·01
Tb	<0·0217	0·251	0·514	0·498	0·403	0·644	0·909	0·692	0·331	0·453	0·653
Tm	<0·0217	0·145	0·292	0·286	0·234	0·346	0·452	0·365	0·0709	0·0828	0·238
Y	0·787	10·00	20·5	20·4	16·7	23·9	32·6	26·2	5·67	7·56	18·7
Yb	0·0988	0·955	1·92	1·92	1·50	2·28	3·03	2·41	0·454	0·505	1·59
Ag	0·0351	0·0820	0·284	0·0681	0·0865	0·121	0·0501	0·0685	0·107	0·143	0·0797
As											
Ba	2·14	21·7	66·5	100·0	446	275	461	253	559	474	667
Bi	<0·025	0·110	0·866	<0·025	<0·025	0·0412	<0·025	0·114	0·219	0·247	0·0396
Cd											
Co	79·5	43·6	97·4	40·5	46·2	40·2	41·9	36·1	24·1	32·1	32·2
Cr	278	682	442	237	553	246	110	157	59·1	65·4	106
Cu	94·2	47·7	483	44·4	20·7	105	29·4	29·5	43·6	61·1	53·2
Ga	4·61	9·90	13·1	14·6	17·3	17·5	24·8	18·4	26·9	25·6	26·2
Ge	1·17	1·09	1·60	1·42	1·56	1·76	2·09	1·80	2·07	2·02	1·62
Hf	0·0313	0·464	1·21	0·753	0·483	0·376	0·198	2·18	0·0290	<0·025	0·0470
Mn	987	760	947	767	950	1070	1030	843	482	541	590
Mo	<0·05	<0·05	<0·05	<0·05	<0·05	<0·05	<0·05	<0·05	<0·05	<0·05	<0·05
Nb	0·280	0·503	1·65	2·04	0·874	2·27	4·94	3·58	6·10	6·81	5·23
Ni	913	92·6	565	106	112	62·2	30·4	35·3	20·4	48·5	69·3
Pb	0·0999	1·08	11·8	4·20	4·79	7·12	8·07	8·18	15·1	14·9	9·52
Rb	0·191	11·2	5·10	15·3	69·0	29·8	34·3	30·6	67·6	69·0	61·0
Sb	<0·025	0·276	<0·025	<0·025	<0·025	<0·025	<0·025	<0·025	<0·025	<0·025	<0·025
Se	<0·5	<0·5	<0·5	<0·5	<0·5	<0·5	<0·5	<0·5	<0·5	<0·5	<0·5
Sn	<0·05	0·465	1·35	1·01	0·383	0·755	0·156	1·09	0·852	0·953	0·845
Sr											
Ta	0·116	0·597	0·188	0·267	0·111	0·253	0·327	0·321	0·491	0·553	0·381

(continued)

Table 2: Continued

Sample:	KR030A	KR006	KR044.3	KR039	KR023	KR011	KR043.2	KR017	HID12a	HID12c	KR071
Rock type:	Cum. gabbro	Gabbro	Gabbro	Gabbro	Gabbro–diorite	Gabbro–diorite	Gabbro–diorite	Diorite	Peralum. tonalite	Peralum. tonalite	Peralum. tonalite
Te	<0·025	<0·025	<0·025	<0·025	<0·025	<0·025	<0·025	<0·025	<0·025	<0·025	<0·025
Ti											
Tl	<0·025	0·0512	<0·025	0·0579	0·279	0·0848	0·171	0·146	0·436	0·442	0·313
W	162	88·6	119	105	76·9	128	153	126	134	141	114
Zn	40·7	35·0	71·2	50·1	57·0	68·6	99·3	71·0	100·0	116	86·5

Sample:	KR026	KR027.2	KR060.1	KR007
Rock type:	Metalum. tonalite	Leuco-granite	Leuco-granite	Leuco-granite
SiO_2	65·8	72·1	74·5	77·9
TiO_2	0·87	0·48	0·25	0·09
Al_2O_3	15·8	15·2	14·2	12·9
Fe_2O_3	5·59	2·11	1·46	0·54
MnO	0·08	0·02	0·02	0·02
MgO	2·27	1·28	0·45	0·34
CaO	3·54	4·03	1·72	0·87
Na_2O	3·74	3·82	4·37	3·48
K_2O	2·37	1·11	2·84	4·35
P_2O_5	0·17	0·14	0·05	0·02
SO_3	0·02			
LOI	0·68	0·50	0·39	0·27
Total	100·9	100·8	100·2	100·8
Ce	24·1	13·2	34·4	34·1
Dy	3·84	1·95	2·49	1·88
Er	2·35	1·14	1·27	0·831
Eu	0·851	0·759	0·407	0·114
Gd	3·37	2·08	2·98	2·74
Ho	0·761	0·396	0·470	0·324
La	9·20	6·14	15·1	14·3
Lu	0·391	0·152	0·154	0·0840
Nd	12·0	6·98	14·3	14·4
Pr	2·81	1·61	3·82	3·94
Sc	23·7	8·32	6·75	2·90
Sm	3·35	1·82	3·17	3·24
Tb	0·591	0·324	0·454	0·376
Tm	0·342	0·158	0·174	0·109
Y	22·8	12·2	14·2	9·28
Yb	2·52	1·04	1·13	0·653
Ag	0·0587	<0·025	<0·025	<0·025
As				
Ba	914	305	584	131
Bi	<0·025	<0·025	<0·025	<0·025
Cd				
Co	32·3	47·0	35·2	33·7
Cr	62·4	7·65	0·213	1·75

(continued)

Table 2: Continued

Sample:	KR026	KR027.2	KR060.1	KR007
Rock type:	Metalum. tonalite	Leuco-granite	Leuco-granite	Leuco-granite
Cu	32·8	6·87	3·57	2·71
Ga	31·4	17·9	23·0	12·4
Ge	1·86	1·13	1·25	1·19
Hf	0·0477	0·0517	0·203	0·0421
Mn	607	145	125	28·5
Mo	<0·05	<0·05	<0·05	<0·05
Nb	6·31	3·27	4·08	1·58
Ni	35·4	37·6	6·26	1·08
Pb	12·9	9·47	16·2	23·1
Rb	63·8	41·2	88·9	76·9
Sb	<0·025	<0·025	<0·025	<0·025
Se	<0·5	<0·5	<0·5	<0·5
Sn	0·366	0·640	2·00	0·145
Sr				
Ta	0·373	0·268	0·461	0·157
Te	<0·025	<0·025	<0·025	<0·025
Ti				
Tl	0·327	0·193	0·401	0·372
W	177	354	295	391
Zn	89·9	28·6	24·1	16·2

Major oxides in wt %; trace elements in ppm. LOI, loss on ignition; b.d., below detection limit. Whole-rock analyses were performed in two separate runs; samples listed up to KR035.2 were prepared in a zirconia mill whereas samples listed from KR030A onwards were prepared in a tungsten carbide mill, and thus the reported values for W and Ta are unreliable.

arc, with enriched large ion lithophile elements (LILE; Rb, Ba, K, Pb, Sr), and depleted high field strength elements (HFSE; Nb, Ta) relative to N-MORB (see Peate *et al.*, 1997). Sulfide-bearing gabbros have sloping light REE (LREE) and flat heavy REE (HREE) patterns, and are enriched in REE relative to the most primitive gabbros (Fig. 9a).

The peraluminous and metaluminous tonalites (~63–70 wt % SiO_2) are clearly delineated by their REE patterns. Peraluminous tonalites have negatively sloped chondrite-normalized REE profiles, with the LREE values mostly above 50 and the heaviest REE values at ~2·5; La/Yb ratios range from 26·9 to 48·3. The peraluminous tonalite profiles have a continuous negative slope from the LREE to the HREE (Fig. 9b). Conversely, the metaluminous tonalites have more variable chondrite-normalized REE profiles sloping negatively from 30–100 in the LREE to 6–10 in the HREE (Fig. 9b); La/Yb ratios range from 3·7 to 17·3. The metaluminous tonalite profiles feature negatively sloping LREE as for the peraluminous tonalites, but the HREE flatten at ~10. The most distinctive feature separating the peraluminous and metaluminous tonalites is the relative HREE enrichment in the latter. This is also reflected in Y contents, an element chemically similar to the HREE, which in metaluminous tonalites is 1·1–3 times greater than in peraluminous tonalites. This may indicate the presence of residual garnet in the source region of the peraluminous tonalites, whereas the metaluminous tonalites may have been extracted from a garnet-free source. The aluminous assemblage of the peraluminous tonalites, containing garnet, orthopyroxene, cordierite, and sillimanite, is consistent with dehydration melting of pelitic metasediments. These minerals may represent peritectic phases that were entrained as the magma escaped its source. In contrast, the hornblende-bearing metaluminous tonalites may have been produced by dehydration melting of intermediate to mafic meta-igneous rocks (this is consistent with the observation of partially melted amphibolites on the southwestern margin of the OGC). Trace amounts of sulfide minerals (~1 vol. %) associated with graphite and ilmenite occur throughout both types of tonalite (Fig. 4). In the nearby Oshirabetsu Gabbroic Complex, which is similar to the OGC, graphite is abundant and has a $\delta^{13}C$ signature (−23·34 to −23·88‰; $\delta^{13}C_{PDB}$) similar to that found in the Nakanogawa Group sediments (about −25·7‰; Tsuchiya *et al.*, 1991).

Diorites (~57 to ~63 wt % SiO_2) are intermediate between the non-troctolite gabbros and the tonalites in terms of major elements, trace elements, and REE chemistry. Diorite REE profiles (Fig. 9c) follow the gabbroic trends, with enriched sloping LREE and flat HREE trends. However, normalized values are above the gabbro values (Fig. 9c).

Sulfur isotopes

The sulfur isotope signature of sulfides from non-troctolite gabbros ($SiO_2 > 45\%$) is highly variable, ranging from +6 to −7·5‰ (relative to Vienna Cañon Diablo Troilite, VCDT; Fig. 10, Table 3). Diorite and tonalite from the OGC have consistently negative values ranging from −4·5 to −10·5‰ (Fig. 10). Mantle sulfur is characterized by $\delta^{34}S_{VCDT}$ values of 0 ± 2‰, implying that some of the sulfur in the gabbros is derived from the tonalites, and ultimately the metasedimentary rocks. Takahashi & Sasaki (1983) reported similar sulfur isotope data for sulfides in the Oshirabetsu Gabbroic Complex to the east of the OGC ($\delta^{34}S_{VCDT} = -5{\cdot}91 \pm 0{\cdot}92$‰), and suggested that their data reflect magmatic assimilation of country rock sedimentary sulfur ranging in $\delta^{34}S_{VCDT}$ between −12·3‰ and −5·3‰. Given that the most primitive non-cumulate gabbros in the OGC have arc-like signatures, and thus were probably derived from a metasomatized mantle wedge, some of this isotopic signature could reflect a slab-derived component of sulfur. However, given the additional evidence for mixing or assimilation of crustal melts (see below), addition of some crustal sulfur via the tonalites (of which there are two types) to the gabbro is likely to have occurred within the OGC. Because the tonalites appear to contain a significant proportion of relict minerals, including sulfides (Fig. 4b), the component of sulfur added to the gabbro via mixing or assimilation from this source is expected to be more than the amount that can be dissolved in a reduced tonalitic melt.

Carbon isotopes

Samples of massive and disseminated sulfide from the Horoman mine were selected for carbon isotope analyses of their contained graphite. Table 4 shows the results of these analyses, which gave $\delta^{13}C$ values ranging from −19·3 to −23·1‰ ($\delta^{13}C_{PDB}$). These data indicate a clearly organic origin for the graphite, which is consistent with its derivation from the tonalites and/or graphitic country rocks, although they are a little higher than the $\delta^{13}C$ value of −25·7‰ obtained by Tsuchiya *et al.* (1991) for the Nakanogawa Group sediments from some distance away. This difference may be due to natural regional variation in the $\delta^{13}C$ signature of the metasedimentary rocks, and possibly partially due to mixing with a small amount of mantle-derived carbon contained within the mafic magmas.

FURTHER EVIDENCE OF ASSIMILATION AND MAGMA MIXING

AFC modelling

The carbon isotope compositions and the abundance of graphite in the mineralized gabbros clearly indicate that gabbro evolution involved assimilation of, or mixing with, a crustal component; this is consistent with the magma mingling features observed in the field and the range of intermediate magma compositions in the OGC. To undertake a first-order analysis of this mixing process, a simple AFC model was constructed (Electronic Appendix 2). In this model, REE concentrations were modelled at progressively increasing F value steps of 0·05 from 0·05 to 1·0, and for r values of 0–0·9 in steps of 0·1, using K_D values taken from Frey (1969), Paster *et al.* (1974), Matsui *et al.* (1977), and Lynton *et al.* (1993). Two primitive non-cumulate gabbros, one from near the Horoman Mine (KR006; Fig. 8) and the other from further away (KR061; Fig. 8), were modelled as the parental mafic magma. Peraluminous or metaluminous tonalites were then mixed with the mafic parent to produce REE profiles at different proportions and degrees of mixing and fractionation. The goal of the modelling was to produce an REE profile of a mixed gabbro + tonalite composition that matched the REE profile of the S-bearing gabbros.

It should be noted that this analysis of mixing and fractional crystallization involving two end-member magmas is a simplification of reality. The OGC system is really a four-component system involving mixing of arc basalt, metaluminous tonalite and peraluminous tonalite, and assimilation of metasediment. Nor did we undertake the energy constrained AFC modelling approach of Spera & Bohrson (2001). The results below are based on an assumed constant crystallizing phase assemblage of plagioclase + olivine + clinopyroxene ± ilmenite. Iterative models accounting for changes in phase stability with progressing crystallization would refine these estimates; however, at such small mixing and fractionation proportions, the bulk chemistry of the evolving magma changes little and therefore the stable crystallizing assemblage would not change significantly. A sensitivity analysis on the K_D values of the REE in each crystallizing phase showed that increases and decreases by one order of magnitude have little effect on the relative proportions of mixing and fractionation estimated by the model (Rebryna, 2009). This means that the model is somewhat insensitive to the input parameters and that the output, therefore, is necessarily limited in scope. However, because the mixing estimates produced by the AFC model are used broadly (i.e. the exact abundances of REE in calculated mixtures are not under scrutiny), these estimates are still useful.

Table 3: Sulfur isotope data ($\delta^{34}S$)

Sample ID	Rock type	Run 1	Run 2	Run 3	Run 4	Run 5	Run 6	Average
Standard								
Blank	Blank	20·28	0·00	0·00	0·00	0·00		
NBS127	Standard	24·06	22·76	23·21	19·94	21·70	24·71	
NBS123	Standard	19·80	19·13	18·62				
Field samples								
KR030A	Cumulate gabbro	−3·66	10·59	18·95	0·23	4·27	1·21	1·90
KR044.1	Gabbro						−7·59	−7·59
KR049	Gabbro	−5·42	4·09			6·06	4·03	5·05
KRO44.3	Gabbro				−4·33	−5·38	−5·62	−5·05
KRO44.3 rep.					−4·50	−5·44		
KR045.2	Gabbro					−0·63	−0·44	−0·53
KR013	Diorite	−5·01	−8·69	−6·12			−10·56	−10·56
KR013 rep.		−5·70	−6·44	−5·54				
HID12c	Peraluminous tonalite	13·02	−5·25	−2·65	−4·84			−4·60
HID12c rep.					−4·35			
KR025.2	Metaluminous tonalite	−0·97		−4·84	−6·83		−7·73	−7·28
KR071	Peraluminous tonalite					−7·94	−9·72	−8·83
KR024	Peraluminous tonalite					−5·44	−7·44	−6·44
KR027.2	Leucogranite dyke		−5·87	2·68				−1·60
KR021	Carbonaceous metased.	−2·13	−10·64	−6·32				−6·36
KR044.2	Sulfide sep. from gabbro		−4·91	−5·76				−5·05
KR044.2 rep.		−3·85	−6·55	−4·17				
KR005	Sulfide sep. from diorite	−3·72	−5·12	−5·07			−10·39	−6·22
KR005 rep.		−6·24	−6·76					

Matrix effects and residual ash affected the values in the first three runs, therefore no correction is available. Runs 4–6 are corrected to the NBS127 standard (accepted value = 20·3). Only the corrected data have been averaged and used to generate Fig. 10.

Table 4: C isotope data for graphite in sulfide-bearing gabbros

Rock ID	$\delta^{13}C‰$	Sample description
KR005	−19·5	Massive sulfide near mine entrance
KR005 r	−19·3	
KR003	−20·0	Disseminated sulfide in gabbro
KR003 r	−20·4	
KR013	−20·1	80–90% sulfide
KR013 r	−19·7	
KR015	−22·8	Disseminated sulfide in gabbro
KR015 r	−23·1	

r, repeat analysis.

AFC model results

For all samples modelled (see Supplementary Data Electronic Appendix 2), the best fit between the averaged chondrite-normalized sulfide-bearing gabbro REE profile and the modeled REE profiles occurs at an r value of 0·7 and $F = 0·80$ (Fig. 11), for mixing between the near mine gabbro sample (KR006) and metaluminous tonalite (KR031). The best fit was determined by least-squares linear regression (the lowest value was 24·5). These r and F values imply that the original magma underwent a large amount of assimilation relative to fractionation. A combination of approximately 9·8 wt % mixing and 14 wt % fractional crystallization results in the REE abundances of the average chondrite-normalized sulfide-bearing gabbro shown in Fig. 11. Mixing between this gabbro and other tonalites generated a poorer fit and required less mixing and fractional crystallization (as low as 3·6% mixing and 12% fractionation). Mixing between the

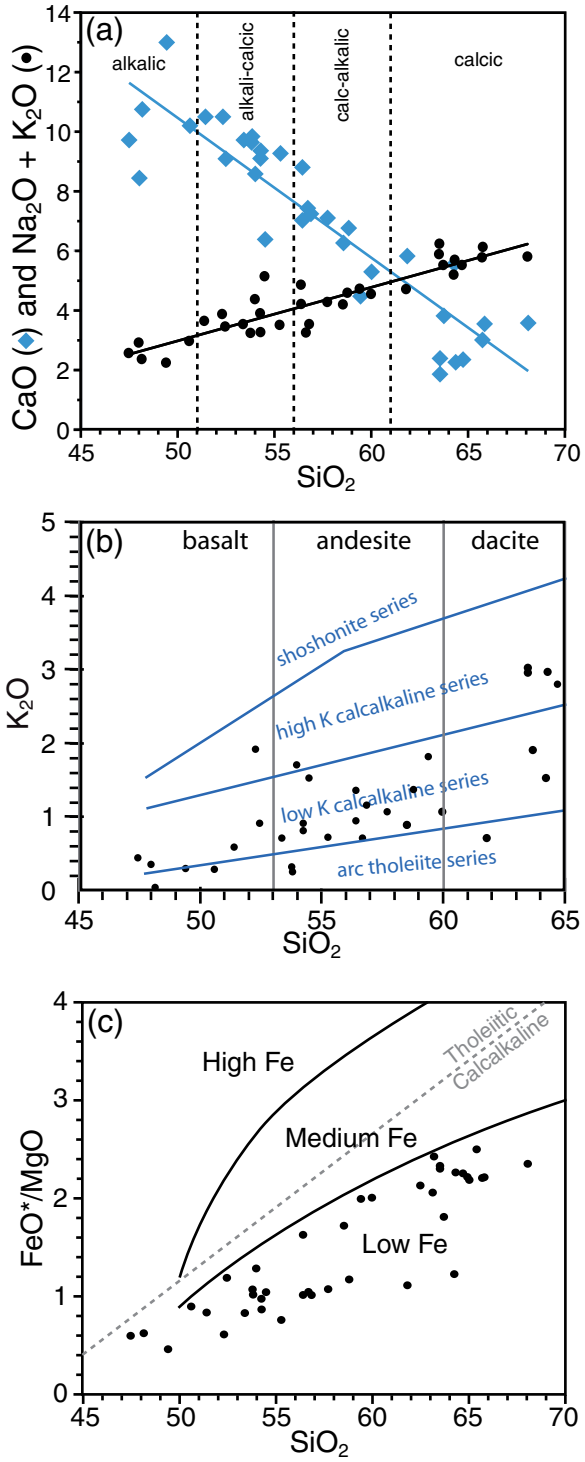

Fig. 6. Geochemistry of bulk-rock samples from the OGC intrusive suite. (a) Comparison of CaO and Na_2O+K_2O vs SiO_2 (wt %). Intersecting trends indicate that the suite is slightly more calcic than calc-alkaline; named fields are after Peacock (1931). (b) K_2O–SiO_2 plot for mafic to intermediate rocks of the OGC, showing that that these are mainly low-K series rocks. (c) FeO*/MgO vs SiO_2 diagram (FeO* is total Fe as FeO) showing that the OGC intrusive rocks belong to the low-Fe suite of Arculus (2003).

distal gabbro sample (KR061) and metaluminous tonalite KR031 generated a similar fit (LSR of 31), and occurs at $r=0{\cdot}8$ and $F=0{\cdot}9$, requiring a combination of 6·4% mixing and 8% fractional crystallization.

Analysis of the change in oxidation state driven by mixing

In a mixing magmatic system consisting of interaction between an oxidized arc basalt and a reduced, graphite-bearing tonalite there will be equilibration of the oxidation state, which is dependent on the proportions of the two end-members in the mixture. It is possible to model how the oxidation state of such a system changes during progressive mixing by taking a redox budget approach, as advocated by Evans (2006) and Evans & Tomkins (2011). In this approach it is recognized that the oxidizing or reducing capacity of both end-members is determined by the quantity of the redox-sensitive elements (in this case Fe, S and C are relevant) and the oxidation state of those elements in each end-member (Evans, 2006). Redox budget calculations basically use a mass-balance approach to determine how much reductant (or oxidant) needs to be added to a rock or melt to reach a given reference state. The redox budget of a geological system was defined by Evans (2006) as the number of moles of electrons that need to be added to the system for it to reach a given reference oxidation state:

$$\mathrm{RB} = \sum_i (n_i v_i) \qquad (1)$$

where RB is the redox budget, n_i is the number of moles of redox state i in the sample of interest, and v_i is the number of electrons needed to take 1 mole of redox state i to the reference redox state.

In the discussion section (see the section 'Reduction-induced sulfide saturation') we are interested in determining how much graphite needs to be added to an oxidized, sulfur-rich arc basalt to (1) reduce it sufficiently to cause sulfide exsolution of magmatic sulfide, and (2) reduce it sufficiently that sulfide exsolution is maximized. We have considered these questions for two hypothetical end-member basalt melts using the bulk composition of mine-proximal gabbro KR006 (Supplementary Data Electronic Appendix 1), one that might be typical of arc basalts with initial oxidation state of FMQ +1·25 and 3000 ppm S (basalt y), and the other an extremely oxidized (FMQ +2) and S-rich (1% S) arc basalt (basalt x). It should be noted that the more oxidized end-member will require more reductant to reach the reference condition. The reductant in the mixed magma system of the OGC was the peraluminous tonalite with entrained graphite. Our model calculates how much graphite would need to be in the tonalite to reduce the mixed magma sufficiently to reach the two reference states identified above, at increments of increasing proportion of tonalite.

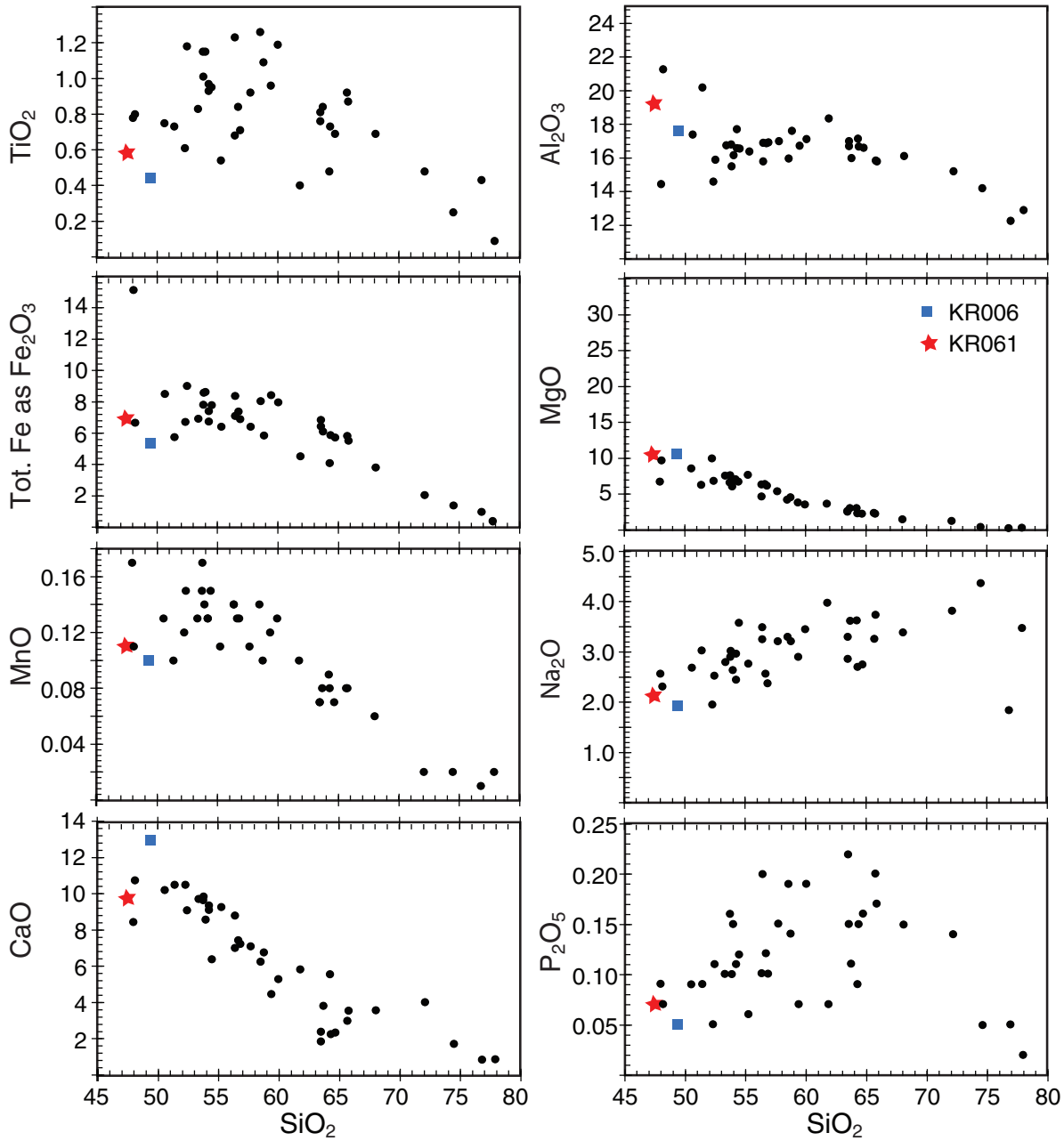

Fig. 7. Harker variation plots of major element oxides against SiO_2 for various intrusive rocks of the OGC. Units are in wt %. The end-member gabbros used in the AFC modelling are represented by the filled square (KR006) and the filled star (KR061).

Relevant components in this redox budget calculation are the relatively high Fe^{3+}/Fe^{2+} ratio and sulfate (S^{6+}) in the basalt end-members (in the model the basalt end-members are considered to have no C), and the comparatively low Fe^{3+}/Fe^{2+} ratio and graphite in the tonalite. The tonalite has a low Fe^{3+}/Fe^{2+} ratio because it was generated during partial melting in equilibrium with graphite, and Fe_{Tot} (reported as Fe_2O_3; Electronic Appendix 1) is slightly less abundant in the tonalite than in the end-member basalts (4·16 wt % and 5·43 wt % Fe_2O_3, respectively). The low Fe^{3+}/Fe^{2+} ratio in the tonalite is important because, being relatively abundant, Fe contributes significantly to the redox budget. Graphite influences the redox state of the mix through oxidation from C to CO_2, which is a four-electron change; reduction of sulfate to sulfide is an eight-electron change and reduction of Fe^{3+} to Fe^{2+} is a one-electron change. In this scenario the redox budget equation becomes

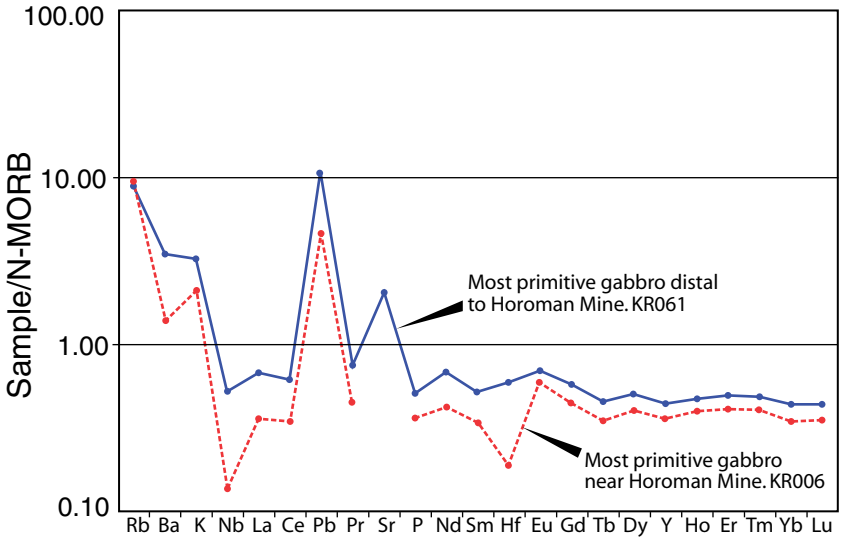

Fig. 8. MORB-normalized multi-element plot showing the composition of primitive gabbros in the OGC. KR006 was sampled several hundred meters from the Horoman Mine, whereas KR061 was collected from several kilometers away. Sr data were not analysed for KR006.

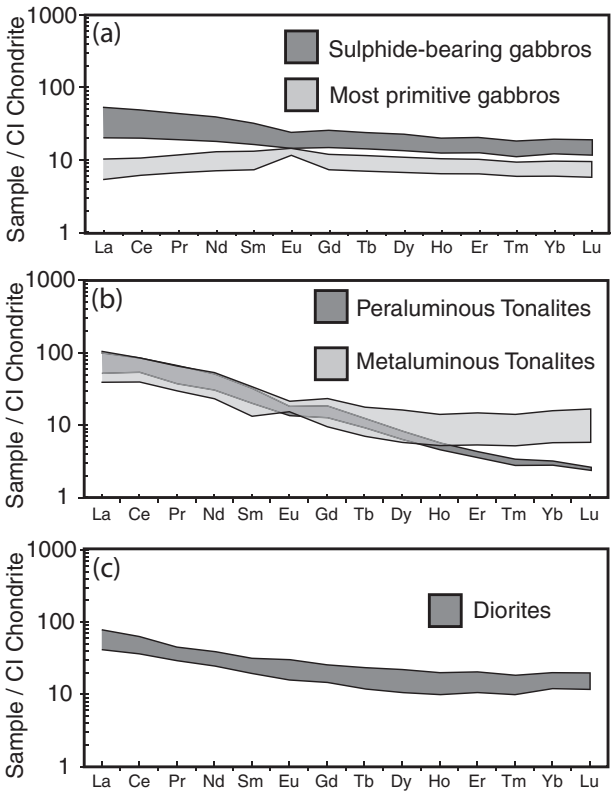

Fig. 9. Chondrite-normalized REE patterns for various intrusive rocks of the OGC. (a) Comparison between the most primitive and sulfide-bearing gabbros. (b) Comparison between per- and metaluminous tonalites. (c) Range of variation in diorites, which are thought to represent the product of mixing between gabbroic and tonalitic magmas.

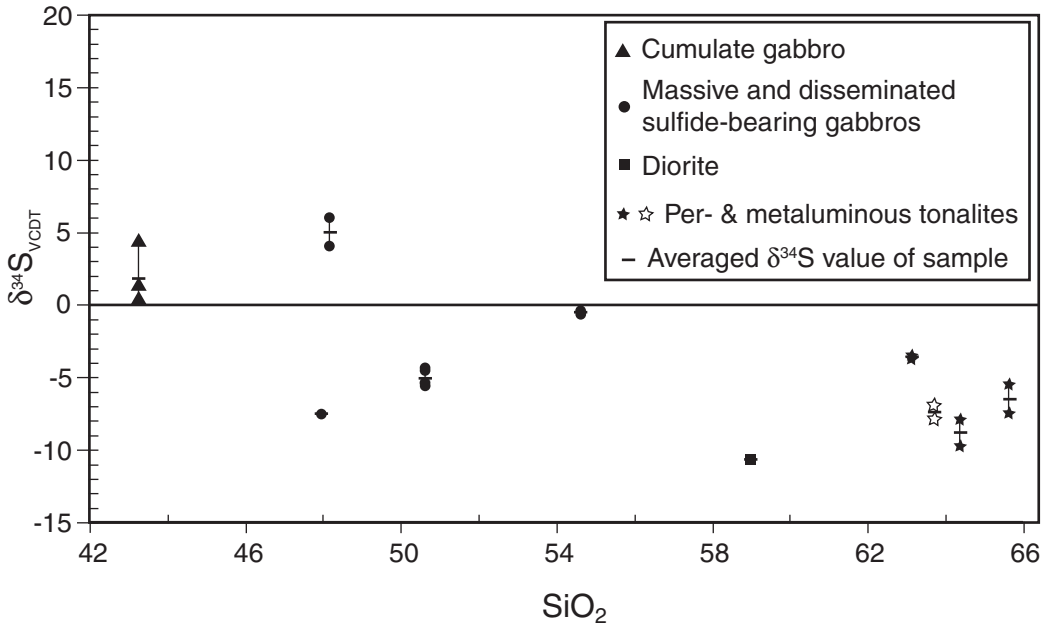

Fig. 10. Variation of $\delta^{34}S_{VCDT}$ in sulfide separates vs SiO_2 of the silicate host rock. The data points indicate repeat analyses of each sample; the dash represents the average value.

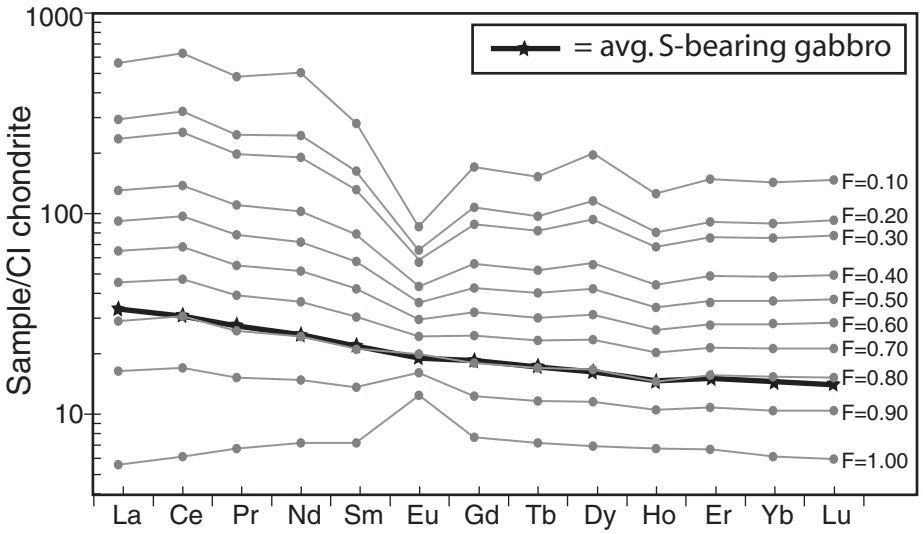

Fig. 11. The best-fit result from the AFC modelling (see the entire range of results in Electronic Appendix 2), which occurs at $r = 0{\cdot}7$. The black curve is the average sulfide-bearing gabbro composition; the labelled grey curves represent the chemistry of the system at varying F values as indicated. Linear regressed best fit is at $F = 0{\cdot}8$.

$$RB = v_{Fe}(n\mathrm{Fe}_i^{3+} - n\mathrm{Fe}_f^{3+}) + 2(n\mathrm{S}_i^{6+} - n\mathrm{S}_f^{6+}) \quad (2)$$

where

$$v_{Fe} = [(n\mathrm{Fe}^{3+}/\sum \mathrm{Fe})_i - (n\mathrm{Fe}^{3+}/\sum \mathrm{Fe})_f]/4 \quad (3)$$

and i and f refer to the initial and final melts respectively. If all of the Fe in the initial basalt was Fe^{3+}, and all of this was reduced to Fe^{2+} through mixing, v_{Fe} would be 0·25 (i.e. one mole of C oxidation requires 4 moles of Fe reduction). However, $Fe^{3+}/\sum Fe$ is <1 in the initial melt, and >0 in the final mixed melt, so v_{Fe} is <0·25. Therefore, for small changes in redox, in systems that contain little sulfate and similar proportions of Fe_{Tot} in the end-member magmas, only a very small proportion of graphite needs to be added, especially where $Fe^{3+}/\sum Fe$ in the reductant is significantly lower than in the oxidant (as in the case envisaged here).

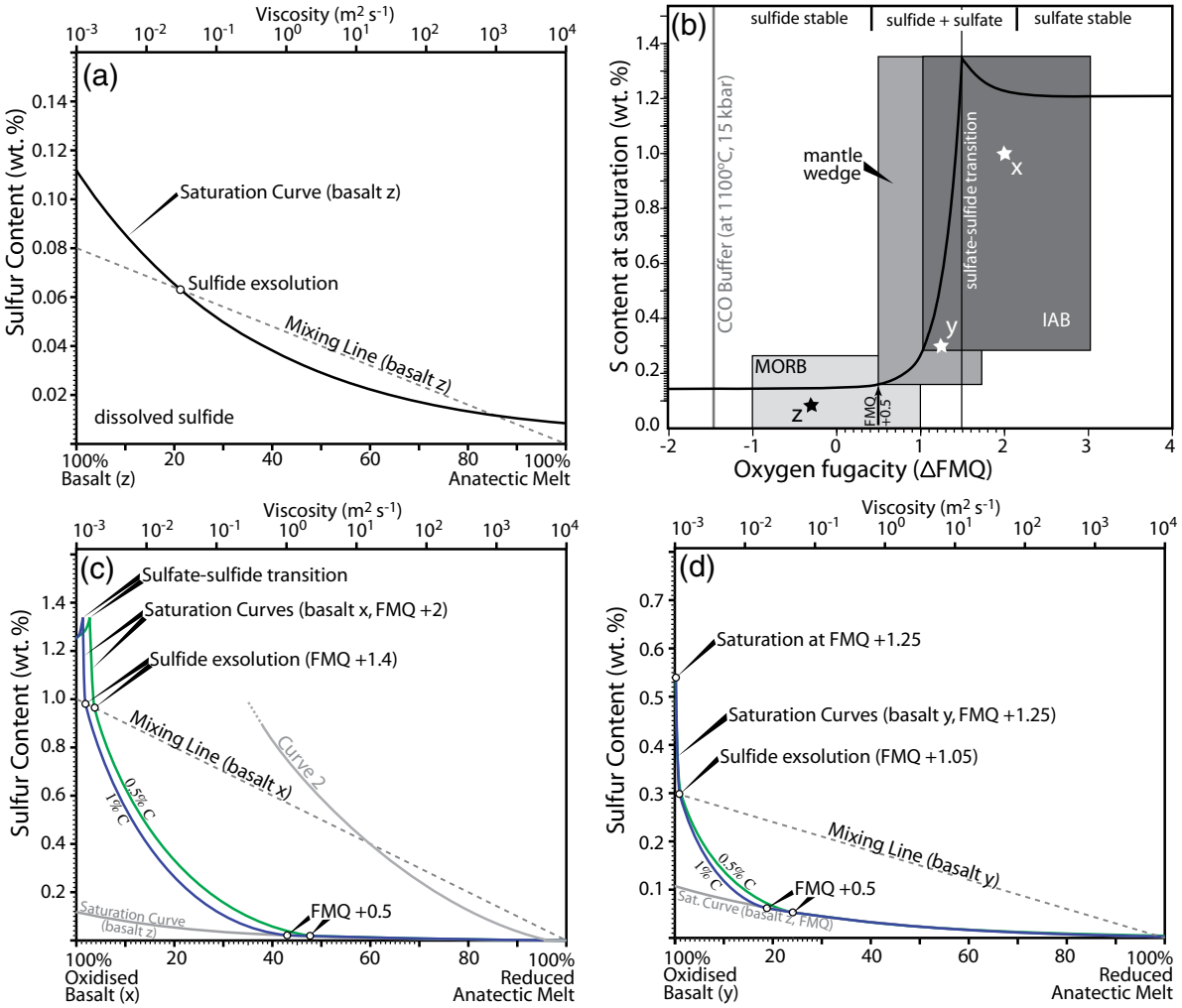

Fig. 12. Variability in sulfide saturation processes in magma mixing systems as a function of oxidation state of the mafic magma. (a) Sulfide saturation curve for mixing between an oxidized basalt and a reduced felsic contaminant. Modified from Li & Ripley (2005). (b) Sulfur content at sulfide saturation in basaltic melts of varying oxidation states (IAB, island arc basalt; modified from Jugo *et al.*, 2010). The three stars labelled x, y and z represent the basalt end-member compositions depicted in parts (a), (c) and (d). The line labelled 'CCO Buffer' represents the oxidation state that a basalt would be buffered towards if graphite was added. (c) Saturation curves that result from contamination of an arc basalt (based on the bulk composition of KR006) containing 1% dissolved sulfur at an initial oxidation state of FMQ +2, with tonalite (based on the bulk composition of KR031) containing 1% graphite and 0·5% graphite. (d) Sulfide saturation curves that result from contamination of a moderately oxidized arc basalt (same bulk composition) containing 3000 ppm dissolved sulfur at an initial oxidation state of FMQ +1·25 with the same tonalite containing 1% graphite and 0·5% graphite. It should be noted that the scales on the *y*-axes are different for each of (a), (c) and (d); the saturation curve from (a) is shown in (c) and (d) for comparison. In both (c) and (d), the positions of the sulfide exsolution points at FMQ +1·4 [in (c)] and FMQ +1·05 [in (d)], and the points where sulfate reduction is complete (FMQ +0·5), were calculated by redox budget modelling (see Supplementary Data Electronic Appendix 3).

The bulk compositions used in the redox budget modelling were from a non-cumulate primitive gabbro close to the Horoman Mine and for a peraluminous graphite-bearing tonalite (sample KR006 for the gabbro end-member, and KR031 for the tonalite end-member), the starting temperatures of the end-members were 1330°C for the gabbro (basalt) and 900°C for the tonalite; the pressure used in the modelling was 15 kbar. The thermodynamic program MELTS (Ghiorso & Sack, 1995) was used to determine the Fe^{3+}/Fe^{2+} ratio in the incremental mixtures.

The calculations and results of the redox budget modelling are contained in Supplementary Data Electronic Appendix 3 and illustrated in Fig. 12. In the case of basalt y (FMQ +1·25), very little graphite was needed in the tonalite to cause sulfide saturation at very low degrees of mixing because only a small change in fO_2 was required, and mixing in of ~19% tonalite containing 1% graphite

(compared with ~24% tonalite containing 0·5% graphite) was needed to maximize sulfide exsolution. Sulfide exsolution is considered to be maximized when all sulfate has been reduced to sulfide (see Fig. 12 and later discussion). In the case of basalt x (FMQ +2), a small amount of mixing was required to induce sulfide saturation (~2% tonalite containing 1% graphite, or ~3·5% tonalite containing 0·5% graphite), and a significant amount was needed to maximize sulfide exsolution (~43% tonalite containing 1% graphite, or ~48% tonalite containing 0·5% graphite).

DISCUSSION

Summary of evidence for magma mixing in the OGC

Several lines of evidence suggest that the gabbroic host to the massive and disseminated sulfides at the Horoman Mine formed in response to magma mixing. Magma mingling textures are widely observed in the field between gabbro and tonalite. Mineral textures in the mineralized gabbro are consistent with the progressive development of chemical instability, which is characteristic of magma mixing. AFC modelling suggests that the sulfide-bearing gabbros have compositions consistent with having evolved through a combination of mixing with addition of ~10 wt % tonalite, and ~14 wt % fractional crystallization. Intermediate intrusive rocks throughout the eastern OGC have major element compositions that plot between the end-member gabbros and tonalites (Fig. 7), consistent with an origin by mixing. The C isotopic composition of graphite in the sulfide-bearing gabbros is consistent with its having been derived from surrounding graphitic metasediments, and both peraluminous and metaluminous tonalites contain significant proportions of graphite. The sulfur isotope compositions of the sulfide-bearing gabbros are consistent with addition of crust-derived sulfur.

Below we present a new model for the formation of magmatic sulfide deposits in the deep crust of subduction-related magmatic arcs, driven by magma mixing.

Reduction-induced sulfide saturation

Ultramafic to mafic magmas must become saturated in sulfide to exsolve sulfide liquids. This can happen by raising the sulfur content of the magma, or by lowering the sulfur content at the sulfide saturation (SCSS) threshold (i.e. by lowering the threshold at which sulfide saturation is reached). A range of processes can lower the SCSS threshold, but one of the most effective is by lowering the FeO content of the magma, which can occur during mixing with a more felsic magma. Figure 12a (modified from Li & Ripley, 2005) illustrates this concept. The curve plotted in this diagram shows a concave-upward decline in S solubility with increasing contamination of the magma with a crustal melt. The superimposed binary mixing line between a sulfur-rich mafic end-member basalt (basalt z) and a sulfur-free felsic end-member suggests that mixing can theoretically cause sulfide saturation in a mixing magma system. The shallowly concave-upward shape of the S saturation curve implies that the amount of mixing required to induce sulfide saturation is sensitive to the starting sulfur content of the mafic end-member.

However, Fig. 12a is drawn for a reduced system. If, instead, we incorporate the knowledge that sulfur is an order of magnitude more soluble in magmas under oxidized conditions (Jugo *et al.*, 2005) and that there is a sharp transition in solubility between sulfide- and sulfate-stable conditions (Fig. 12b; modified from Jugo, 2009), the shape of the saturation curve can be significantly different. Figure 12c shows sulfide saturation curves for mixing between a highly oxidized and S-rich arc basalt (basalt x) and a reduced crust-derived felsic magma containing either 1% graphite or 0·5% graphite. The proportions of mixing required to reach sulfide liquid exsolution at FMQ +1·4, and to maximize sulfide exsolution at FMQ +0·5 (these ΔFMQ values are derived from Fig. 12b), were calculated by redox budget modelling (see Supplementary Data Electronic Appendix 3). The positive jump and then large drop shown on the sulfide saturation curves in Fig. 12c represent the transition between sulfate- and sulfide-stable conditions (equivalent to the rising and then steeply dropping transition moving from right to left on Fig. 12b). This abruptness of this transition varies as a function of the redox balance between the two mixing end-members, so the more graphite-rich tonalite induces sulfide exsolution at lower proportions of mixing. In this very oxidized system, the amount of mixing required and the probability of sulfide exsolution is comparatively insensitive to the starting sulfur content of the mafic end-member (compared with Fig. 12a).

In perhaps the majority of natural arc systems the oxidation state of the primitive arc basalts intruding into a lower crustal MASH zone will not be entirely in the sulfate stability field (basalt x in Fig. 12c has a sulfate-stable oxidation state). Island arc basalts are, however, typically oxidized relative to FMQ (Fig. 12b). Figure 12d represents the situation for what might be a more typical arc basalt (basalt y), which has an oxidation state that plots within the transition zone between sulfide and sulfate stability. Redox budget calculations show that the steep part of the saturation curve in Fig. 12d is close to the 100% basalt axis because little reductant needs to be added to it to bring its oxidation state far enough back towards a reduced state (i.e. towards basalt z on Fig. 12b) to induce saturation. This is because in this range of oxidation state, sulfur solubility changes rapidly with only small changes in fO_2. Based on the findings of Jugo (2009), any basalt more oxidized than FMQ +0·5 should be susceptible to this enhanced sulfide saturation potential during mixing with

a felsic magma with significant reducing potential. Thus, our central hypothesis is that magmatic sulfide mineralization can form in MASH zones within the lower arc crust through reduction of oxidized arc basalt via magma mixing and/or assimilation of crust-derived material that has a significant reducing potential. We refer to this process as reduction-induced sulfide saturation. This process has similarities to the magnetite crisis model of Jenner *et al.* (2010), in which magnetite crystallization from oxidized basaltic magma triggers reduction of the melt and sulfide exsolution.

Examination of the hypothesis based on observations of the OGC

The sulfur isotope signature of the Horoman magmatic sulfides ($\delta^{34}S = -5{\cdot}46 \pm 1{\cdot}16‰$) is consistent with addition of a component of crustal sulfur to the gabbro through magma mixing and assimilation, given that mantle-derived sulfur has a $\delta^{34}S$ signature of $0 \pm 2‰$, although an arc basalt could potentially contain a component of slab-derived sulfur. Sulfur addition has been demonstrated to have caused sulfide saturation and ultimately ore formation at many other magmatic sulfide occurrences (see reviews by Arndt *et al.*, 2005; Barnes & Lightfoot, 2005). However, if crust-derived sulfur is added to an oxidized arc basalt, with a high capacity for dissolved sulfur, this alone may not be enough to induce sulfide or sulfate saturation. In these magmas, reduction is also likely to be needed.

It is clear that the primary controls on sulfide solubility (temperature, pressure, SiO_2 content, and Fe^{2+} content; see O'Neill & Mavrogenes, 2002) are modified during magma mixing. However, the processes driving a magma to become reducing and sulfide stable from an oxidized state containing dissolved sulfate must rely on the addition of components to the system that have a strong effect on oxygen fugacity. One such component is graphite, which is commonly produced by metamorphism of organic-rich sediments and clearly survives the process of partial melting and migmatization of the lower crust (e.g. see Pattison, 2006).

The process of partial melting and extraction of melts from migmatites permits retention of a significant component of unmelted crustal material in the escaping felsic magma (e.g. Clarke, 2007; Tomkins *et al.*, 2009). The observation of enclaves of migmatite in the tonalites (Fig. 3b), and numerous peritectic garnet, cordierite, and orthopyroxene xenocrysts in the peraluminous tonalites, shows that this has occurred in the OGC. Graphite in particular is expected to be easily extracted from migmatites because it has low density ($\sim 2{\cdot}2\ g\ cm^{-3}$) and typically has plate-like crystal morphologies that are easily carried by flowing material (e.g. Figs 4 and 5). That graphite extraction in migmatite-derived melts has occurred in the OGC is evidenced by observations of common graphite flakes within tonalite (Fig. 4), and by $\delta^{13}C$ signatures of the graphite in disseminated and massive gabbro sulfides that have a distinctly organic signature typical of the Nakanogawa Group sediments. Thus, crust-derived graphite was added to mafic magma via magma mixing within the OGC.

Figure 12b shows the position of the graphite buffer relative to FMQ and the oxidation state of island arc basalts (at higher temperatures it plots off the diagram to the left). Addition of graphite to an arc basalt would drive its oxidation state towards the CCO buffer and would continue to do so until all the added graphite was consumed. The sulfide-bearing gabbro in the OGC contains a significant proportion of graphite, which our AFC modelling suggests was added by mixing with ~10% graphite-bearing, crust-derived tonalite; its oxidation state has thus been set to the CCO buffer through magma mixing. Unfortunately, we do not know the oxidation state of the parental end-member mafic magma to the sulfide-bearing gabbro, so we cannot be completely certain that reduction-induced sulfide saturation was responsible for formation of the Horoman sulfide deosits. None the less, this location does demonstrate that the physical processes involved in magma mixing in MASH zones can do everything physically needed to form magmatic sulfides via reduction-induced sulfide saturation.

The occurrence of carbonaceous metasediments in the lower arc crust is ideal for our model of reduction-induced sulfide saturation, but not simply through providing a source of graphite as a reductant. Carbonaceous metasediments are also typically enriched in sulfur relative to other rock types, so presumably anatectic melts derived from them would also be relatively sulfur rich (see Tomkins *et al.*, 2009), and this is the case with the tonalites in the OGC (Fig. 4b). Adding sulfur to a mixing magmatic system that is approaching sulfide saturation would accelerate the onset of saturation. Thus, in this system there are multiple mechanisms driving rapid onset of sulfide saturation.

The position and slope of the sulfate–sulfide transition in Fig. 12c and d depend on how much reductant needs to be added to the highly oxidized arc basalt to sufficiently lower its oxidation state. Graphite is a highly effective redox buffer, but it may not be present in many MASH zones. In systems that lack graphite, the oxidation state will probably be dominated by equilibration between Fe^{2+} and Fe^{3+} in the mafic magma and the added crustal component. Although the redox state of the lower crust may typically be lower than the fO_2 of the sulfate–sulfide transition, the redox potential of melt derived from it is likely to be moderate to low, depending on the iron content, which can be low in many felsic anatectic melts. Thus, the sulfate–sulfide transition for MASH zone magma mixing in systems that involve low-Fe, graphite-free anatectic melts may plot in a position closer to that shown for

Curve 2 in Fig. 12c. In such a system, sulfide exsolution would occur in intermediate mixed magmas, rather than mafic compositions, if at all. These low-Fe, graphite-free systems may allow the mixed magma to remain significantly oxidized, and thus metal- and sulfur-rich.

Consequences of reduction-induced sulfide saturation for ore genesis

Oxidation of the mantle wedge via fluids liberated from a subducting slab converts some mantle sulfide to sulfate, allowing higher sulfur solubility in the resultant basaltic melt (Mungall, 2002*b*; Jugo, 2009). Relatively low degrees of mantle melting would thus be needed to consume all the mantle sulfur not shielded as inclusions in residual mantle minerals (see Fig. 12b), even at mild degrees of elevated oxidation, allowing formation of a more sulfur- and metal-enriched basaltic magma than would be possible in more reduced settings (Jugo, 2009). The redox state of the mantle wedge in subduction zones is thought to range from FMQ + 0·3 to FMQ + 2·0 (Parkinson & Arculus, 1999). Thus, oxidized arc basalts may typically contain higher sulfur and metal contents than other basalts. A feature of our model is that only relatively mildly sulfur-enriched basalts are needed for reduction-induced sulfide saturation to work (Fig. 12c and d). Therefore, whether sulfides can exsolve in a MASH zone environment may be more a function of there being an effective crust-derived reductant, rather than needing an unusually sulfur-enriched arc basalt.

One of the distinct features of a magma mingling and mixing environment is that it can rapidly generate a system that is out of chemical equilibrium. Our model indicates that mixing can potentially generate a sudden high degree of sulfide supersaturation for a wide range of starting basalt sulfur contents (see Fig. 12c and d). Supersaturation develops in geological systems that experience an abrupt change in solubility (volcanic systems are a common example), and may be particularly relevant in magmatic sulfide systems owing to the high surface tension between sulfide and silicate melt, which may inhibit nucleation (Mungall, 2002*a*). In the system modelled here, only small increments of mixing are required to induce large changes in S solubility, so high degrees of supersaturation are anticipated. The greater the extent of sulfide supersaturation, the more pervasive the consequent sulfide globule nucleation, such that a high degree of sulfide supersaturation leads to a high number density of sulfide melt globules (Mungall, 2002*a*). A term known as the R factor describes the volume of silicate melt that a given sulfide globule chemically interacts with (see Campbell & Naldrett, 1979; Mungall, 2002*a*), such that a high R factor sulfide globule interacts with a large volume of silicate melt relative to its own volume. Because chalcophile metals partition strongly from silicate melts into sulfide melts, high R factor sulfide droplets are rich in Cu, Ni, PGE and Au relative to those with low R factor. A system with a high degree of supersaturation forms a high number density of sulfide globules and is likely to develop a relatively low overall R factor (Mungall, 2002*a*). This is because closely spaced sulfide droplets are expected to compete with each other for diffusive sequestration of chalcophile metals, and thus the effective ratio of sulfide volume to silicate volume is likely to be higher than otherwise. Therefore, in the system described here, the metal tenor (the proportion of metal) in any resulting sulfide accumulation within the magma chamber may be lower than in magmatic sulfide deposits formed in other settings. In addition, the silicate magma in such a highly supersaturated system would experience a more efficient and complete scavenging of metals, because a higher proportion of silicate melt would chemically interact with sulfide melt.

The growth of single sulfide globules is governed by interplay between diffusion, the absolute amount of sulfur in the system and the number density of sulfide globules, such that widely spaced globules in sulfur-rich magma will grow to reach larger sizes than closely spaced globules. This is because closely spaced, high number density globules will quickly develop sulfur diffusion haloes that interact and therefore compete with their neighbours for a finite supply of sulfur (Mungall, 2002*a*), although this model does not take into consideration coalescence of closely spaced globules. Therefore, our system that generates a high degree of sulfide supersaturation is expected to form abundant, closely spaced, and thus small, sulfide droplets. Smaller sulfide globules that do not coalesce are more likely to be retained within migrating silicate magma because of their lower Stoke's Law settling velocities. Thus, there is potential for MASH zone systems to act as staging chambers that supply dykes rich in small sulfide droplets to higher levels in the crust, where changes in magma flow velocity can lead to sulfide accumulation. Such a process can lead to development of higher R factors, through the prolonged interaction between sulfide droplets and silicate melt along tortuous flow pathways, and has been implicated in the formation of important ore deposits such as at Voisey's Bay in Newfoundland, Canada (Mungall, 2002*a*).

A further consequence of this process is that efficient depletion of batches of silicate magma in chalcophile and siderophile elements would inhibit formation of ore deposits in the upper arc crust, such as porphyry Cu–(Au–Mo) deposits and related skarn and epithermal Au–Ag systems. This efficient silicate magma depletion would occur where sulfide saturation is reached when the hybrid magma is still relatively mafic and has low enough viscosity to allow sulfide melt globules to settle out (as at the Horoman Mine). However, in those systems where sulfide saturation occurs after magma mixing has developed more intermediate hybrid magma compositions, the

viscosity of the magma may be too great for efficient sulfide settling to occur, thereby inhibiting formation of a magmatic sulfide accumulation. This appears to have been the case in many places within the eastern OGC, where sparsely disseminated spherical sulfide globules are commonly observed in the diorites. Thus, there must be a limit (on the *x*-axis of Fig. 12c and d) on the amount of contamination of the mafic magma, beyond which the hybrid magma will be viscous enough to retain sulfide melt globules as it escapes the lower crust.

There are likely to be many regions of deep arc crust that do not contain carbonaceous metasediments, and magmas generated therein may not have the reducing potential needed to induce sulfide saturation during mixing with oxidized basaltic magma. In these systems, the hybrid magmas remain oxidized enough to retain high sulfur and metal contents and those magmas that escape the lower crust may go on to form porphyry Cu–(Au–Mo) and related deposits in the upper arc crust. In this way, arc-hosted magmatic sulfide deposits of the type envisaged here, and porphyry Cu–(Au–Mo) and related ore systems, can be viewed as end-members of a spectrum of ore-forming processes related to arc magmatism.

We suggest that the ideal settings for the formation of large magmatic sulfide ore deposits in the lower arc crust include the following features. The ideal magma mixing system would be located in the deepest levels of the arc crust because such a setting would allow insulation of the system at higher temperatures for longer, promoting more effective magma mixing on a larger scale, and providing time for convection and settling of sulfide melt droplets. The oxidation state of the arc basalt would ideally be at or just below the sulfate–sulfide transition (ΔFMQ of about +1·5; Jugo *et al.*, 2010). This basalt would have been generated by low-degree partial melting of the mantle wedge, to a degree just sufficient to dissolve all mantle sulfide into the melt, ensuring that it is metal-rich and close to sulfide saturation when emplaced into the lower crust. The lower crust would ideally contain a high proportion of sulfidic carbonaceous shale. These features would ensure widespread onset of a high degree of sulfide supersaturation at only low degrees of crustal contamination, when the hybrid magma has a sufficiently low viscosity to allow settling out of the sulfide droplets.

How widespread could this process be?

Whether this process of reduction-induced sulfide saturation is common to many deep arc MASH complexes will be controlled by the abundance of deep crust material with high reducing potential. If graphitic metasediments are a widespread feature of deep arc crust globally, then mixing between oxidized arc basalt and reduced lower crustal material would be common. Exposed island arc sequences commonly have associated accretionary wedge complexes, which are a combination of arc-derived sediments and ocean floor sediments scraped off the down-going slab at a subduction margin. Total carbon in oceanic floor sediments is highly variable and factors that favour high carbon content in deep-sea sediments are high organic productivity in the overlying waters (e.g. along coasts and at upwelling sites), high input of terrigenous organic matter (e.g. at fluvial deltas), and rapid burial rate (e.g. in turbidites; Stein, 1990). These conditions are common features in arcs.

Where accretionary wedge sediments form part of the stratigraphy of accreted arc sequences, such as in the Hidaka Metamorphic Belt, Talkeetna Arc, and Kohistan Sequence, there is significant potential for under-plating mafic melts to induce partial melting of graphitic accretionary wedge sediments. Along the margin of the paleo-Japan arc, for example, it is likely that all of these conditions were met: a coastal environment, terrigenous sediment input from erosion of the arc, and the formation of turbidites (Nanayama *et al.*, 1993). The OGC is emplaced within graphitic metasediments, now migmatites, of the Nakanogawa Group, a Paleocene sequence of turbidites (Nanayama *et al.*, 1993) that are part of the Hidaka Supergroup, which is thought to be an accretionary wedge complex. Therefore, we suggest that mixing of arc basalt with graphitic crust-derived felsic magmas, or assimilation of graphitic metasediments, may be a widespread feature of deep arc crust. This may partly explain why porphyry Cu–(Au–Mo) and related ore deposits are typically not found in arc segments dominated by reduced intrusive complexes.

The interpretation that the lowermost crust of the Hidaka Metamorphic Belt (HMB) sequence has delaminated (Tsumura *et al.*, 1999) is consistent with the lack of extensive cumulate piles or layered mafic intrusions in the HMB sequence. The Talkeetna Arc Section in Alaska is a more complete sequence, continuous from peridotitic upper mantle to layered gabbroic intrusions to upper crustal volcanic rocks (Greene *et al.*, 2006). The Kohistan sequence in Pakistan includes at its base a series of layered mafic and ultramafic intrusions (Treloar *et al.*, 1996), but is without a mantle peridotite sequence as in the Talkeetna section and HMB. The HMB sequence does have many components similar to those of the Talkeetna section, but not in such an uninterrupted sequence. It has fault-bound mantle peridotites and faulted ophiolites present, but these are not conformable with the bottom of the sequence. It is therefore apparent that in most instances some truncation is to be expected and that an entirely uninterrupted conformable sequence from upper mantle to upper crust is exceptionally rare. Even in the otherwise complete Talkeetna section, delamination of the lower crust is invoked to account for an apparent volumetric lack of pyroxenite (Greene *et al.*, 2006). Truncation may therefore be common in obducted arc sequences, which may also

explain the rarity of these sequences in the rock record globally. Thus, although the process of reduction-induced sulfide saturation may occur deep within many arcs, the magmatic sulfide accumulations that this process generates may be exposed at the surface only relatively rarely.

However, given the potential of crustal MASH zones to act as staging chambers, higher level magmatic sulfide accumulations may be a common feature of these systems. A possible example of such a higher level system is the Duke Island Complex, which developed in an arc setting in southeastern Alaska (Thakurta *et al.*, 2008). Here, magmatic sulfides are associated with olivine clinopyroxenites, which contain crust-derived graphite and sulfur, thought to have been introduced by assimilation of carbonaceous shales. The genesis of the Aguablanca arc-hosted magmatic sulfide deposit in Spain may have involved assimilation of sulfidic black shales (Casquet *et al.*, 2001), and thus may fit our model, but again there is no information on the pre-contamination oxidation state of the mafic magma. Deposits that form at higher crustal levels have a greater probability of being exposed at the surface, so these are perhaps better exploration targets.

CONCLUSIONS

(1) The Opirarukaomapu Gabbroic Complex represents an example of mixing between mantle-derived basaltic and crust-derived, graphite- and sulfur-bearing tonalitic magmas. This mixing promoted sulfide saturation and accumulation of exsolved sulfide melt at relatively low degrees of contamination of the mafic magma.

(2) We have developed a model for reduction-induced sulfide saturation and consequent magmatic sulfide ore deposit formation involving mixing between oxidized, and therefore sulfur- and metal-rich, arc basalt and reduced crust-derived magma. The proposed magma mixing process has the potential to induce high degrees of sulfide supersaturation with significant consequences for the metallogeny of arcs.

(3) The evidence contained in the OGC indicates that the physical processes needed to drive reduction-induced sulfide saturation can occur in the deep crust of magmatic arcs.

(4) Reduction-induced sulfide saturation can drive formation of magmatic sulfide deposits in the deep to middle arc crust, and at the same time inhibit formation of porphyry Cu–(Au–Mo) and related deposits in the upper crust. Lack of reduction-induced sulfide saturation permits formation of porphyry Cu–(Au–Mo) and related deposits, and thus in arcs, magmatic sulfide and porphyry Cu-related deposits can be viewed as end-members in a spectrum of magmatic processes.

(5) The observed scarcity of magmatic Ni–Cu sulfide deposits in arc settings is likely to be due to the rarity of exposures of the deeper parts of the arcs where these deposits form. Thus, if examples of deep arc sections can be found, which contain exposures of carbonaceous metasediments, these are considered to be highly prospective for Ni–Cu mineralization.

ACKNOWLEDGEMENTS

We thank in particular Ryo Anma and Hiroyuki Kamiyama for assistance during the planning and execution stages of fieldwork in Japan, and subsequently with various enquiries. Ian Nichols and Louise Edwards are thanked for editing and helpful comments regarding the igneous petrology. Katy Evans is gratefully acknowledged for guidance on the initial stages of the redox budget modelling. Pedro Jugo, John Brophy, an anonymous reviewer, and Editor Ron Frost are thanked for their insightful and helpful comments, which promoted significant improvement of the paper.

FUNDING

Funding was provided by a Monash University Fellowship to A.G.T. and an AusIMM Bicentennial Gold 88 Endowment award to K.C.R.

SUPPLEMENTARY DATA

Supplementary data for this paper are available at *Journal of Petrology* online.

REFERENCES

Arculus, R. J. (2003). Use and abuse of the terms calcalkaline and calcalkalic. *Journal of Petrology* **44**, 929–935.

Arndt, N. T., Lesher, C. M. & Czamanske, G. K. (2005). Mantle-derived magmas and magmatic Ni–Cu–(PGE) deposits. *Economic Geology 100th Anniversary Volume* 5–23.

Barnes, S.-J. & Lightfoot, P. C. (2005). Formation of magmatic nickel sulfide deposits and processes affecting their copper and platinum group elements. *Economic Geology 100th Anniversary Volume* 179–213.

Campbell, I. H. & Naldrett, A. J. (1979). The influence of silicate:sulfide ratios on the geochemistry of magmatic sulfides. *Economic Geology* **74**, 1503–1506.

Carroll, M. R. & Rutherford, M. J. (1985). Sulfide and sulfate saturation in hydrous silicate melts. *Journal of Geophysical Research* **90**, C601–C612.

Carroll, M. R. & Rutherford, M. J. (1987). The stability of igneous anhydrite: Experimental results and implications for sulfur behavior in the 1982 El Chichon trachyandesite and other evolved magmas. *Journal of Petrology* **28**, 781–801.

Casquet, C., Galindo, C., Tornos, F., Velasco, F. & Canales, A. (2001). The Aguablanca Cu–Ni ore deposit (Extremadura, Spain), a case of synorogenic orthomagmatic mineralisation: Age and isotope composition of magmas (Sr, Nd) and ore (S). *Ore Geology Reviews* **18**, 237–250.

Chapman, M. E. & Solomon, S. C. (1976). North American–Eurasian plate boundary in northeast Asia. *Journal of Geophysical Research* **81**, 921–930.

Clark, I. D. & Fritz, P. (1997). *Environmental Isotopes in Hydrogeology*. New York: Lewis.

Clarke, D. B. (2007). Assimilation of xenocrysts in granitic magmas: Principles, processes, proxies, and problems. *Canadian Mineralogist* **45**, 5–30.

Evans, K. A. (2006). Redox decoupling and redox budgets: Conceptual tools for the study of earth systems. *Geology* **34**, 489–492.

Evans, K. A. & Tomkins, A. G. (2011). The relationship between subduction zone redox budget and arc magma fertility. *Earth and Planetary Science Letters* **308**, 401–409.

Frey, F. A. (1969). Rare earth element abundances in a high-temperature peridotite intrusion. *Geochimica et Cosmochimica Acta* **33**, 1429–1447.

Funahashi, M. & Igi, S. (1956). *Explanatory text of the geological map of Japan, Horoizumi*. Tsukuba: Geological Survey of Japan, 76 p.

Ghiorso, M. S. & Sack, R. O. (1995). Chemical mass transfer in magmatic processes IV. A revised and internally consistent thermodynamic model for the interpolation and extrapolation of liquid–solid equilibria in magmatic systems at elevated temperatures and pressures. *Contributions to Mineralogy and Petrology* **119**, 197–212.

Goldschmidt, V. M. (1937). The principles of distribution of chemical elements in minerals and rocks. *Journal of the Chemical Society* 655–673.

Greene, A. R., DeBari, S. M., Kelemen, P. B., Blusztajn, J. & Clift, P. D. (2006). A detailed geochemical study of island arc crust: The Talkeetna Arc Section, south–central Alaska. *Journal of Petrology* **47**, 1051–1093.

Haughton, D. R., Roeder, P. L. & Skinner, B. J. (1974). Solubility of sulfur in mafic magmas. *Economic Geology* **69**, 451–467.

Honma, H. (1997). Petrological characteristics of Opirarukaomappu Plutonic Complex in the southern Hidaka Metamorphic Belt, Hokkaido, Japan. *Memoirs of the Geological Society of Japan* **47**, 43–55.

Ishihara, S. & Terashima, S. (1985). Cenozoic granitoids of central Hokkaido, Japan—An example of plutonism along collision belt. *Bulletin of the Geological Survey of Japan* **36**, 653–680.

Jenner, F. E., O'Neill, H. S. C., Arculus, R. J. & Mavrogenes, J. A. (2010). The magnetite crisis in the evolution of arc-related magmas and the initial concentration of Au, Ag and Cu. *Journal of Petrology* **51**, 2445–2464.

Jugo, P. J. (2009). Sulfur content at sulfide saturation in oxidized magmas. *Geology* **37**, 415–418.

Jugo, P. J., Luth, R. W. & Richards, J. P. (2005). An experimental study of the sulfur content in basaltic melts saturated with immiscible sulfide or sulfate liquids at 1300°C and 1·0 GPa. *Journal of Petrology* **46**, 783–798.

Jugo, P. J., Wilke, M. & Botcharnikov, R. E. (2010). Sulfur K-edge XANES analysis of natural and synthetic basaltic glasses: Implications for S speciation and S content as function of oxygen fugacity. *Geochimica et Cosmochimica Acta* **74**, 5926–5938.

Kamiyama, H., Nakajima, T. & Kamioka, H. (2007). Magmatic stratigraphy of the tilted Tottabetsu Plutonic Complex, Hokkaido, north Japan: Magma chamber dynamics and pluton construction. *Journal of Geology* **115**, 295–314.

Kato, N., Sato, H., Orito, M., Hirakawa, K., Ikeda, Y. & Ito, T. (2004). Has the plate boundary shifted from central Hokkaido to the eastern part of the Sea of Japan? *Tectonophysics* **388**, 75–84.

Kemp, A. I. S., Shimura, T. & Hawkesworth, C. J. (2007). Linking granulites, silicic magmatism, and crustal growth in arcs: Ion microprobe (zircon) U–Pb ages from the Hidaka metamorphic belt, Japan. *Geology* **35**, 807–810.

Kiminami, K., Niida, K., Ando, H., Kito, N., Iwata, K., Miyashita, S., Tajika, J. & Sakakibara, M. (1992). Cretaceous–Paleogene arc–trench systems in Hokkaido. In: Adachi, M. & Suzuki, K. (eds) *29th IGC Field Trip Guide Book*. Nagoya: Nagoya University, pp. 1–43.

Kimura, G. (1986). Oblique subduction and collision: Forearc tectonics of the Kuril arc. *Geology* **14**, 404–407.

Komatsu, M., Osanai, Y., Toyoshima, T. & Miyashita, S. (1989). Evolution of the Hidaka metamorphic belt, northern Japan. In: Daly, J. S., Cliff, R. A. & Yardley, B. W. D. (eds) *Evolution of Metamorphic Belts: Proceedings of the 1987 Joint Meeting of the Metamorphic Studies Group and IGCP Project 235*. London: Geological Society, pp. 487–493.

Komatsu, M., Toyoshima, T., Osanai, Y. & Arai, M. (1994). Prograde and anatectic reactions in the deep arc crust exposed in the Hidaka metamorphic belt, Hokkaido, Japan. *Lithos* **33**, 31–49.

Kress, V. (1997). Magma mixing as a source for Pinatubo sulphur. *Nature* **389**, 591–593.

Li, C. & Ripley, E. M. (2005). Empirical equations to predict the sulfur content of mafic magmas at sulfide saturation and applications to magmatic sulfide deposits. *Mineralium Deposita* **40**, 218–230.

Li, C., Maier, W. D. & de Waal, S. A. (2001). The role of magma mixing in the genesis of PGE mineralization of the Bushveld Complex; thermodynamic calculation and new interpretations. *Economic Geology* **96**, 653–662.

Luhr, J. F. (1990). Experimental phase relations of water-saturated and sulfur-saturated arc magmas and the 1982 eruptions of El Chichon volcano. *Journal of Petrology* **31**, 1071–1114.

Lynton, S. J., Candela, P. A. & Piccoli, P. M. (1993). An experimental study of the partitioning of copper between pyrrhotite and a high silica rhyolitic melt. *Economic Geology* **88**, 901–915.

MacLean, W. H. (1969). Liquidus phase relations in the FeS–FeO–Fe_3O_4–SiO_2 system, and their application in geology. *Economic Geology* **64**, 865–884.

Maeda, J. & Kagami, H. (1996). Interaction of a spreading ridge and an accretionary prism: Implications from MORB magmatism in the Hidaka magmatic zone, Hokkaido, Japan. *Geology* **24**, 31–34.

Malaviarachchi, S. P. K., Makishima, A., Tanimoto, M., Kuritani, T. & Nakamura, E. (2008). Highly unradiogenic lead isotope ratios from the Horoman peridotite in Japan. *Nature Geoscience* **1**, 859–863.

Matsui, Y., Onuma, N., Nagasawa, H., Higuchi, H. & Banno, S. (1977). Crystal structure control in trace element partition between crystal and magma source. *Bulletin de la Société Française de Minéralogie et de Cristallographie* **100**, 315–324.

Mavrogenes, J. A. & O'Neill, H. S. C. (1999). The relative effects of pressure, temperature and oxygen fugacity on the solubility of sulfide in mafic magmas. *Geochimica et Cosmochimica Acta* **63**, 1173–1180.

Mungall, J. E. (2002*a*). Kinetic controls on the partitioning of trace elements between silicate and sulfide liquids. *Journal of Petrology* **43**, 749–768.

Mungall, J. E. (2002*b*). Roasting the mantle: Slab melting and the genesis of major Au and Au-rich Cu deposits. *Geology* **30**, 915–918.

Naldrett, A. J. (2004). *Magmatic Sulfide Deposits: Geology, Geochemistry, and Exploration*. Berlin: Springer.

Nanayama, F., Kanamatsu, T. & Fujiwara, Y. (1993). Sedimentary petrology and paleotectonic analysis of the arc–arc junction: The Paleocene Nakanogawa Group in the Hidaka Belt, central Hokkaido, Japan. *Palaeogeography, Palaeoclimatology, Palaeoecology* **105**, 53–69.

O'Neill, H. S. C. & Mavrogenes, J. A. (2002). The sulfide capacity and the sulfur content at sulfide saturation of silicate melts at 1400°C and 1 bar. *Journal of Petrology* **43**, 1049–1087.

Owada, M., Osanai, Y., Shimura, T., Toyoshima, T. & Katsui, Y. (2003). Crustal section and anatexis of lower crust due to mantle flux in the Hidaka metamorphic belt, Hokkaido, Japan. In:

Arima, M., Nakajima, T. & Ishihara, S. (eds) *Hutton Symposium V, Field Guidebook*. Tsukuba: Geological Survey of Japan, pp. 81–102.

Palyanov, Y. N., Borzdov, Y. M., Khokhryakov, A. F., Kupriyanov, I. N. & Sobolev, N. V. (2006). Sulfide melts–graphite interaction at HPHT conditions: Implications for diamond genesis. *Earth and Planetary Science Letters* **250**, 269–280.

Parkinson, I. J. & Arculus, R. J. (1999). The redox state of subduction zones: Insights from arc-peridotites. *Chemical Geology* **160**, 409–423.

Paster, T. P., Schauwecker, D. S. & Haskin, L. A. (1974). The behavior of some trace elements during solidification of the Skaergaard layered series. *Geochimica et Cosmochimica Acta* **38**, 1549–1577.

Pattison, D. R. M. (2006). The fate of graphite in prograde metamorphism of pelites: An example from the Ballachulish aureole, Scotland. *Lithos* **88**, 85–99.

Peach, C. L., Mathez, E. A. & Keays, R. R. (1990). Sulfide melt–silicate melt distribution coefficients for noble metals and other chalcophile elements as deduced from MORB: Implications for partial melting. *Geochimica et Cosmochimica Acta* **54**, 3379–3389.

Peacock, M. A. (1931). Classification of igneous rock series. *Journal of Geology* **39**, 54–67.

Peate, D. W., Pearce, J. A., Hawkesworth, C. J., Colley, H., Edwards, C. M. & Hirose, K. (1997). Geochemical variations in Vanuatu arc lavas: The role of subducted material and a variable mantle wedge composition. *Journal of Petrology* **38**, 1331–1358.

Piña, R., Romeo, I., Ortega, L., Lunar, R., Capote, R., Gervilla, F., Tejero, R. & Quesada, C. (2010). Origin and emplacement of the Aguablanca magmatic Ni–Cu–(PGE) sulfide deposit, SW Iberia: A multidisciplinary approach. *Geological Society of America Bulletin* **122**, 915–925.

Rebryna, K. C. (2009). Magma mixing and sulfide production in the lower crust: Insights into arc metallogenesis, PhD thesis, Monash University, Melbourne, Vic., 178 pp.

Shiba, M. & Morinaga, K. (1998). Shear movement which formed mylonites around the Opirarukaomappu Gabbro Complex in the southern part of the Hidaka Metamorphic Belt. *Bulletin of the Faculty of Science and Technology, Hirosaki University* **1**, 27–35.

Shimura, T., Komatsu, M. & Iiyama, J. T. (1991). Genesis of the lower crustal garnet orthopyroxene tonalites (S-type) of the Hidaka Metamorphic Belt, Northern Japan. In: Brown, P. E. & Chappell, B. W. (eds) *The Second Hutton Symposium on the Origin of Granites and Related Rocks, Canberra, Australia*, Vol. 83, Transactions of the Royal Society of Edinburgh, Earth Sciences, pp. 259–268.

Spera, F. J. & Bohrson, W. A. (2001). Energy-constrained open-system magmatic processes I: General model and energy-constrained assimilation and fractional crystallization (EC-AFC) formulation. *Journal of Petrology* **42**, 999–1018.

Stein, R. (1990). Organic carbon content/sedimentation rate relationship and its paleoenvironmental significance for marine sediments. *Geo-Marine Letters* **10**, 37–44.

Takahashi, T. & Sasaki, A. (1983). Isotopic composition of sulfur in the Oshirabetsu gabbroic complex and the associated nickeliferous pyrrhotite ore—Magmatic sulfide mineralization and the external source of sulfur. *Mining Geology* **33**, 399–409.

Tarkian, M. & Stribrny, B. (1999). Platinum-group elements in porphyry copper deposits: A reconnaissance study. *Mineralogy and Petrology* **65**, 161–183.

Thakurta, J., Ripley, E. M. & Li, C. (2008). Geochemical constraints on the origin of sulfide mineralization in the Duke Island Complex, southeastern Alaska. *Geochemistry, Geophysics, Geosystems* **9**, Q07003, doi:07010.01029/02008GC001982.

Tomkins, A. G., Weinberg, R. F. & McFarlane, C. R. M. (2009). Preferential magma extraction from K- and metal-enriched source regions in the crust. *Mineralium Deposita* **44**, 171–181.

Treloar, P. J., Petterson, M. G., Jan, M. Q. & Sullivan, M. A. (1996). A re-evaluation of the stratigraphy and evolution of the Kohistan arc sequence, Pakistan Himalaya: Implications for magmatic and tectonic arc-building processes. *Journal of the Geological Society, London* **153**, 681–693.

Tsuchiya, N., Suzuki, S. & Chida, T. (1991). Origin of graphite in the Oshirabetsu gabbroic body, Hokkaido, Japan. *Journal of Mineralogy, Petrology and Economic Geology* **86**, 264–272.

Tsumura, N., Ikawa, H., Ikawa, T., Shinohara, M., Ito, T., Arita, K., Moriya, T., Kimura, G. & Ikawa, T. (1999). Delamination-wedge structure beneath the Hidaka collision zone, Central Hokkaido, Japan inferred from seismic reflection profiling. *Geophysical Research Letters* **26**, 1057–1060.